

Self-similar relativistic blast waves with energy injection

Hendrik van Eerten^{1*} †

¹ *Max-Planck-Institut für Extraterrestrische Physik, Giessenbachstraße 1, 85748 Garching, Germany*

24 February 2014

ABSTRACT

A sufficiently powerful astrophysical source with luminosity depending on time according to a power law will give rise to a self-similar relativistic blast wave with a reverse shock traveling into the ejecta and a forward shock moving into the medium surrounding the source. Once energy injection ceases and the last energy is delivered to the shock front, the blast wave will transit into another self-similar stage where the dynamics are shaped only by the total amount of energy injected.

I describe the evolution of limited duration energy injection blast waves and their transition stage, with an emphasis on the optical / X-ray plateau phase of Gamma-ray Burst (GRB) afterglows as an application. A complete fluid profile during injection including the reverse shock region is given. The transition is shown with one-dimensional simulations of radial flow to take about a sound crossing time. While energy injection is ongoing, the sideways flux of energy due to jet expansion usually lies orders of magnitude below the injected energy, causing the flow to remain approximately radial.

For synchrotron emission from shock-accelerated particles, the resulting flux equations are provided for general circumburst medium structure. The relative flux between forward and reverse shock region depends on their respective magnetizations and the Lorentz factor of the inflowing matter from the source, but for typical afterglow values it is shown that emission from the reverse shock can easily dominate, especially when different degrees of magnetization for both regions are taken into account. After energy injection has ceased, the post-plateau flux will steepen while the reverse shock region dissipates, and drop to the flux level predicted for impulsive injection. Reverse shock emission supports the observational F-t correlation between flux and time at the end of the GRB afterglow plateau phase. During energy injection, the synchrotron injection break for the reverse shock region is shifted to high frequencies due to its strong dependence on the Lorentz factor of the inflowing relativistic wind. These effects are illustrated for typical afterglow values and the specific cases of short GRBs 090515 and 120521A.

Scale invariance of the flux and of the dynamics between different energies and circumburst densities remain unchanged between the different stages of the blast wave evolution, allowing for a straightforward extension of simulation-based fit methods for decelerating blast waves to include the plateau stage.

Key words: plasmas - radiation mechanisms: non-thermal - shock waves - gamma-rays: bursts - gamma-rays: theory

1 INTRODUCTION

Some cataclysmic astrophysical events, such as the merger of neutron stars (Eichler et al. 1989; Paczynski 1991) or the collapse of a very massive star (Woosley 1993; Paczynski 1998; MacFadyen & Woosley 1999), can give rise to brief flashes of gamma rays (‘gamma-ray bursts’, or GRBs) that can be detected at cosmological distances. A common fea-

ture of GRB models is the launch of collimated relativistic ejecta that interact with the surrounding medium and produce an afterglow signal that can be detected from X-rays to radio as the blast wave decelerates.

The classical fireball model for the afterglow (e.g. Meszaros, Laguna & Rees 1993; Meszaros & Rees 1997a) describes the relativistic hydrodynamical evolution after a mass and energy (10^{48-51} erg, depending on the progenitor type) are injected effectively instantaneously into a small region. The fireball expands, accelerates and ultimately decelerates, by sweeping up external matter, with

* Alexander von Humboldt Fellow

† e-mail: hveerten@mpe.mpg.de

a self-similar relativistic fluid profile first described by Blandford & McKee (1976) (hereafter denoted BM76). This deceleration phase might be preceded by a brief phase where a reverse shock runs into the original ejecta (see e.g. Sari & Piran 1995; Sari 1997; Kobayashi, Piran & Sari 1999). The main observed emission component is synchrotron radiation from shock-accelerated electrons interacting with small-scale shock-generated magnetic fields, giving rise to a broadband signal that follows a power-law decay (or rise, at low observer frequencies) in time (e.g. Blandford & McKee 1977). Standard GRB afterglow theory has recently been reviewed by various authors, including Piran (2004); Mészáros (2006); Granot (2007); Van Eerten (2013).

Since the launch of *Swift* (Gehrels et al. 2004), early time plateau phases of shallow decay in afterglow X-ray light curves have been revealed to be far more common than originally expected. These plateaus are commonly attributed to prolonged injection of energy (see e.g. Nousek et al. 2006; Zhang et al. 2006), which can take different forms, such as ejecta with a range of velocities catching up with the shock front (e.g. Rees & Meszaros 1998; Panaitescu, Meszaros & Rees 1998; Sari & Mészáros 2000), long-term luminosity of the source (e.g. Zhang & Mészáros 2001) or conversion of Poynting flux from the ejecta (e.g. Usov 1992; Thompson 1994; Meszaros & Rees 1997b; Lyutikov & Blandford 2003). When the blast wave is continuously driven from the back, the impulsive energy injection scenario no longer correctly describes the fluid evolution and the blast wave will decelerate more slowly or not at all. Instead, for the duration of injection of energy, a more complex system of shocks will form similar to the brief reverse shock stage for massive ejecta, with a contact discontinuity separating the ejecta from the swept-up ambient medium and a reverse shock running into the ejecta, in addition to the forward shock running into the medium that is also present in the impulsive injection scenario.

The exact location and nature of emission during the plateau phase is still not fully resolved. The observed emission will be a mixture of forward and reverse shock contributions, and either can be dominant (see e.g. Zhang & Mészáros 2001; Zhang et al. 2006; Nousek et al. 2006; Butler & Kocevski 2007). Treatments of outflows with a long-lived reverse shock have shown that it is possible to account for a significant part of the overall observed flux and light curve features by emission from the reverse shock region (Uhm 2011; Uhm et al. 2012; Leventis, Wijers & van der Horst 2014). Another strong indication that forward shock emission alone is insufficient to explain observations is the abrupt drop in luminosity that is sometimes seen at the end of the plateau phase (e.g. Troja et al. 2007; Rowlinson et al. 2013).

In this study I consider the dynamics, evolution and emission from energy injection by a power law luminosity from the central source, which includes and generalizes the ‘thick-shell’ case for massive ejecta. In the case of a sufficiently long-lived reverse shock that has become relativistic in the frame of the inflowing fluid, the full reverse shock / forward shock profile is self-similar and treated generally by BM76 (who omit only the reverse shock region density profile). Separate self-similar solutions exist in the literature (e.g. Nakamura & Shigeyama 2006;

Nakayama & Shigeyama 2005), but for our purpose, the radial flow with relativistic reverse shock described in BM76 is sufficient. Since the injection of energy still lasts only for a limited time, the transition from sustained to effectively impulsive injection (i.e. when the injection timescale becomes negligible again compared to the explosion duration) is discussed in detail, including a numerical hydrodynamics approach. Flux equations are derived for the emission that show the relative contributions from forward and reverse shock regions. These equations can be applied directly to observational X-ray and optical data. The reverse shock emission is found to often be important, as is demonstrated using ‘typical’ long GRB afterglow parameters and short GRBs 090515 and 120521A.

In section 2, the self-similar fluid profile during energy injection from a power-law luminosity source is derived and placed in the context of the fireball model. In section 3, the transition after cessation of energy injection is discussed both analytically and numerically (using the RAM relativistic hydrodynamics code, Zhang & MacFadyen 2006). Flux equations and the role of the reverse shock region for the observed emission are treated in section 4, including an application to GRBs 090515 and 120521A. A general discussion follows in section 5, a summary in section 6, and some technicalities are deferred to appendices. Throughout the paper, I discuss how self-similar energy injection blast waves emission fits within the framework of scale-invariant afterglow light curves and simulation-based approaches to data analysis (Van Eerten, van der Horst & MacFadyen 2012; Van Eerten & MacFadyen 2012).

In a separate study, Leventis, Wijers & van der Horst (2014) also find an important role for the reverse shock emission in shaping the observed flux. They consider a homogeneous shell model for long-lived reverse shocks and assume a homogeneous circumburst medium, whereas this study considers a generic power law medium, a full self-similar fluid profile and also examines the transition following energy injection using numerical simulations. Earlier work by Uhm et al. (2012) considers the case where energy injection results from shells with a range of Lorentz factors catching up with the forward shock. There, the fluid profile is not self-similar but calculated in detail using the ‘mechanical model’ approach to afterglow blast waves from Beloborodov & Uhm (2006).

2 SELF-SIMILAR SOLUTION FOR RELATIVISTIC BLAST WAVE WITH ENERGY INJECTION

In this section, I discuss the dynamics of purely radial flow during energy injection.

2.1 Free-flowing relativistic wind

I take as starting point a prolonged injection of energy at time t_{in} at initial radius R_0 , according to

$$L = L_0 t_{in}^q. \quad (1)$$

At the same time matter is injected according to

$$L_M = L_{M,0} t_{in}^q. \quad (2)$$

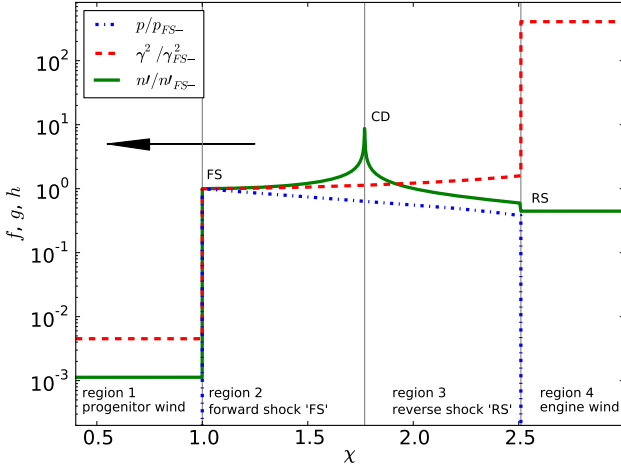


Figure 1. Self-similar fluid profile for a blast wave in a stellar wind environment ($k = 2$) and continuous energy injection $q = 0$. In region 2, the profiles as shown above are equivalent to self-similar functions f , g , h . In region 3, f , g are still equivalent to what is plotted, while the density profile differs from self-similar function H by a normalization factor. At fixed time t we have $dr/ct = -d\chi/2\Gamma^2$. The direction of the blast wave is to the left. The relative values outside of the shocked region and across the contact discontinuity (for the density) are set according to the typical values discussed in section 2.4. In a stellar wind environment, the fluid profile as plotted here remains completely unchanged over time.

In case of a collimated outflow, these injection rates refer to *isotropic equivalent* luminosities, since at early stages the flow is purely radial. These generalize the impulsive injection of the fireball scenario, for which $L \rightarrow L\delta(t - t_0)$ and $L_M \rightarrow L_M\delta(t - t_0)$. When the time evolutions of mass and energy injections are the same, the ratio between L and L_M is given by a fixed $\eta \equiv L/L_M c^2$, again generalizing $\eta \equiv E/Mc^2$ for the fireball, where E the total explosion energy, M the total explosion mass and c the speed of light. I will consider only cases where the baryon loading is small, and $\eta \gg 1$. This injection will result in a relativistic wind, for which

$$r^2 \rho \gamma, \quad r^2 p^{3/4} \gamma, \quad \text{and} \quad r^2 (4p + \rho) \gamma^2 = \text{constant}, \quad (3)$$

along each null flow line of each fluid element, due to conservation of mass, energy and momentum. Here ρ is comoving density, γ the Lorentz factor, r the radius and p the pressure. In the fireball case, these conservation laws only reflect the evolution of an extremely thin outer shell (Piran, Shemi & Narayan 1993; Kobayashi, Piran & Sari 1999), for prolonged energy injection they provide the full profile in the region where the outflow can expand freely. At small radii the outflow is extremely hot, so eqs. 3 imply

$$\gamma \propto r, \quad \rho \propto r^{-3}, \quad p \propto r^{-4}, \quad (4)$$

while at large radii

$$\gamma = \text{constant}, \quad \rho \propto r^{-2}, \quad p \propto r^{-8/3}. \quad (5)$$

(Goodman 1986; Paczynski 1986; Shemi & Piran 1990; Kobayashi, Piran & Sari 1999).

If we combine eqs. 3 with the constraints that the total energy and mass in the expanding sphere (with radius $R \approx$

ct) should be equal to the total energy and mass that have been injected, we obtain

$$\gamma = r/R_0, \quad \rho = \frac{L_M R_0}{4\pi c r^3}, \quad p = \frac{L R_0^2}{16\pi c r^4}. \quad (6)$$

At a radius $R_L \equiv \eta R_0$, all internal energy in the outflow is converted into kinetic energy and the outflow will eventually proceed with fixed Lorentz factor according to

$$\gamma = \eta, \quad \rho = \frac{L_M}{4\pi c \eta r^2}, \quad p = \frac{L R_0^{2/3}}{16\pi c \eta^{4/3} r^{8/3}}. \quad (7)$$

These equations describe the fluid profile for a freely expanding outflow in a dilute medium. However, in reality the expansion does not occur in a total vacuum and at the surface of the sphere a termination shock profile is formed consisting of a reverse shock (RS) moving into the freely expanding ejecta (but still moving outward in the ‘lab’ frame centered on the origin of the explosion), a contact discontinuity (CD) separating the wind from the environment and a forward shock (FS) moving into the circumburst environment, likely a stellar wind profile shaped by the progenitor system or a homogenous interstellar medium (ISM) type profile.

A self-similar profile for the RS-CD-FS system is provided by Blandford & McKee (1976) for the case of a relativistic FS and relativistic RS. In BM76, the density profile inside of the contact discontinuity is not discussed, and indeed most information about the flow can be derived assuming only eq. 1, while remaining agnostic about the mass flux (eq. 2). I review their results below, while adding the full mass profile as determined by the freely expanding wind crossing the RS.

In the remainder of this article I will use the following notation. When a subscript ‘RS’ is attached to a variable, this variable is evaluated at the position of the RS (e.g. r_{RS} for the RS radius). Additionally, in order to avoid ambiguity at fluid discontinuities, a subscript ‘RS+’ is used to refer to a position $r \downarrow r_{RS}$, while a subscript ‘RS-’ refers to $r \uparrow r_{RS}$. The same notation is used for the CD and FS. The phrasing *behind the shock* refers to the downstream, shocked region, while *ahead of the shock* refers to the upstream, unshocked region. For the RS, *behind the shock* therefore refers to the region at $r > r_{RS}$. I will also refer to the various regions using the numbers shown in Figs. 1 and 2.

2.2 Self-similar blast wave with energy injection

In BM76, the similarity variable is given by

$$\chi = [1 + 2(m + 1)\Gamma^2](1 - r/ct), \quad (8)$$

for a blast wave with a forward shock Lorentz factor Γ evolving in time t according to

$$\Gamma^2 \propto t^{-m}. \quad (9)$$

Inverting eq. 8 to obtain the radius for a given χ value gives

$$r = ct(1 - \chi[2(m + 1)\Gamma^2]^{-1}), \quad (10)$$

to $O(\Gamma^{-2})$. The factor m depends on q and k via $m = (2 - q - k)/(2 + q)$, where k describes the slope of the circumburst density profile into which the relativistic outflow expands, according to $\rho = \rho_{ref}(r/r_{ref})^{-k}$. Combining the shock-jump

conditions for a strong relativistic forward shock with the assumption of self-similarity we obtain

$$\begin{aligned} p &= \frac{2}{3}\omega_{FS+}\Gamma^2 f(\chi), \\ \gamma^2 &= \frac{1}{2}\Gamma^2 g(\chi), \\ n' &= 2n_{FS+}\Gamma^2 h(\chi), \end{aligned} \quad (11)$$

between the FS and the CD, where the self-similar functions obey $f(1) = g(1) = h(1) = 1$ at the shock front and χ increases further downstream. For a cold medium, enthalpy $\omega_{FS+} = \rho_{FS+}c^2$. The prime on the number density n' refers to the frame at which the origin of the explosion is at rest (i.e. the frame of the circumburst medium or ‘lab’ frame) and is related to the comoving number density n according to $n = \gamma^{-1}n'$. Mass and number density are related via $\rho = m_p n$ where m_p the proton mass. The self-similar functions can be expressed as differential equations when combining eqs. 11 with the equations of relativistic fluid dynamics. For the Lorentz factor we have:

$$\frac{d \ln g}{d\chi} = g \frac{(7m+3k-4) - (m+2)g\chi}{(m+1)(4-8g\chi+g^2\chi^2)}. \quad (12)$$

Note that the velocity profile does not depend on any of the other fluid quantities. The self-similar equation for pressure is:

$$\frac{d \ln f}{d\chi} = g \frac{4[2(m-1)+k] - (m+k-4)g\chi}{(m+1)(4-8g\chi+g^2\chi^2)} \quad (13)$$

Note that the RHS of the equation contains only g and χ , not f , since the fluid is relativistically hot. BM76 provide complete analytical solutions to the differential equations.

In the case of the Lorentz factor and pressure, these solutions can be applied directly to both regions 2 and 3, since these quantities are continuous across the CD. For the density we have

$$\begin{aligned} \frac{d \ln h}{d\chi} &= g[(m+1)(2-g\chi)(4-8g\chi+g^2\chi^2)]^{-1} \times \\ &\quad [2(9m+5k-8) - 2(5m+4k-6)g\chi + \\ &\quad (m+k-2)g^2\chi^2]. \end{aligned} \quad (14)$$

Note that like the pressure profile, the density profile depends only on χ and the velocity profile.

According to eq. 10, the forward shock radius R is given by

$$R = ct(1 - [2(m+1)\Gamma^2]^{-1}) \approx ct. \quad (15)$$

The forward shock Lorentz factor can be shown to be given by

$$\Gamma^2 = \left[\frac{L_0 \chi_{RS}^{1+q} c^{k-5}}{2^q (m+1)^q 16\pi \rho_{ref} r_{ref}^k f_{RS}} \right]^{\frac{1}{2+q}} t^{\frac{q+k-2}{2+q}}, \quad (16)$$

by equating the energy influx through the RS to the total energy in the RS and FS region. For given q, k , the positions of the CD and RS are fixed in self-similar coordinates and can be shown to be given by $g(\chi_{CD})\chi_{CD} = 2$ and $g(\chi_{RS})\chi_{RS} = 4$. The former follows from the constraint that all fluid elements outside of the CD have to originate at the shock front, the latter from the assumption of a relativistic reverse shock (in the frame of the inflowing wind). Energy

and matter injected at time t_{in} reach the reverse shock at radius R_{RS} at time

$$t = R_{RS}/c + t_{in}, \quad (17)$$

leading to

$$t = t_{in} 2(m+1)\Gamma_{RS}^{-1}. \quad (18)$$

For the reverse shock we have $\Gamma_{RS} = \Gamma/\sqrt{\chi_{RS}}$ and

$$\bar{\Gamma}_{RS} = \frac{1}{2} \left(\frac{\Gamma\sqrt{\chi_{RS}}}{\gamma_{RS-}} + \frac{\gamma_{RS-}}{\Gamma\sqrt{\chi_{RS}}} \right), \quad (19)$$

in the frame of the inflowing material at r_{RS-} (i.e. directly ahead of the RS shock front), denoted with a bar.

2.3 The full density profile

In terms of $x \equiv g\chi$, the solution to the density profile equation 14 is given by

$$h(x) = C \times A(x)^{-\gamma_2} \times B(x)^{\mu_1/\gamma_1} \times (2-x)^{-\mu_2}. \quad (20)$$

Here $A(x)$ and $B(x)$ are functions of x obeying $A(1) = B(1) = 1$, while $\gamma_1, \gamma_2, \mu_1$ and μ_2 are determined by k and q . All these symbols are defined in appendix A. C is a constant of integration whose value is determined by the boundary conditions. In the FS region, $C = 1$, from $h(1) = 1$. However, at the CD the RS region is disconnected from the forward region. Extending the solution from BM76, we define a second function $H(x)$ to describe the self-similar profile in the RS region:

$$H(x) = C_1 \times A(x)^{-\gamma_2} \times B(x)^{\mu_1/\gamma_1} \times (x-2)^{-\mu_2}, \quad (21)$$

which differs from $h(x)$ by a constant factor that is chosen such that $H_{RS+} \equiv 1$. In some cases (e.g. the wind case with $q = 0, k = 0, m = 1$), the density profile singularity at the CD has density going up to infinity. This represents a breakdown of the underlying assumption $p \gg \rho c^2$, meaning that the self-similar solution therefore already ceases to be valid in the vicinity of this point and not just at the singularity itself.

The shock jump condition for the number density behind the (assumed relativistic) reverse shock is given by:

$$\bar{n}_{RS+} = 2n_{RS-}\bar{\Gamma}_{RS}^2, \quad (22)$$

where n_{RS-} the number density of the inflowing material before it crosses the reverse shock (comoving, so denoting it with a bar would be redundant). This can be expressed in the lab frame as:

$$n'_{RS+} = 2n_{RS-}\gamma_{RS-}, \quad (23)$$

where γ_{RS-} the Lorentz factor of the inflowing material in the lab frame. Here however we did use the assumption that $\gamma_{RS-} \gg \Gamma_{RS}$, a condition that is not met when $R \rightarrow R_0$ but easily met later on.

By construction, the density profile throughout the RS region is therefore given by

$$n' = 2n_{RS-}\gamma_{RS-}H(x), \quad (24)$$

where we maintain $x \equiv g\chi$ also throughout the RS region.

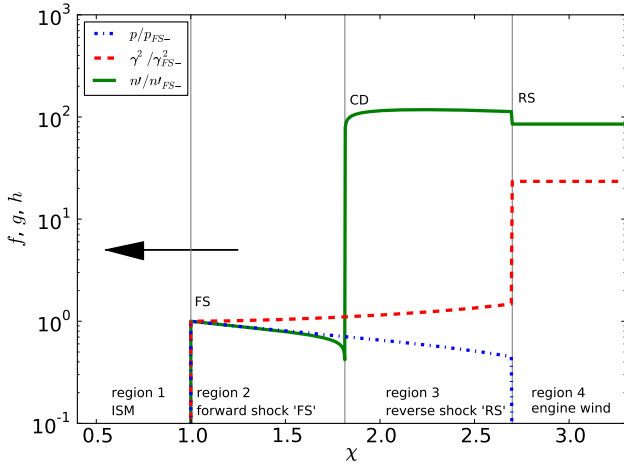


Figure 2. Self-similar fluid profile for a blast wave expanding in a homogeneous medium ($k = 0$) and with constant energy injection ($q = 0$). The relative density difference between forward and reverse shock regions depends on time. For this figure we have used the ISM values described in section 2.4, with time $t = 10^4$ seconds. The interpretation of the fluid profile in terms of self-similar functions f , g , h and H is the same as in Fig. 1.

A quantity of interest is the ratio between densities behind the forward and reverse shock:

$$\begin{aligned} \frac{n'_{RS+}}{n'_{FS-}} &= \frac{\rho_{RS-} \gamma_{RS-}}{\Gamma^2 \rho_{FS+}} \\ &= \frac{L_0}{4\pi \rho_{ref} c^{5-k} R_{ref}^k \eta} \times t_{in}^q \times t^{k-2} \times \Gamma^{-2} \\ &= \frac{1}{\eta} \left[\frac{2^q c^{k-5} f_{RS}^{1+q} L_0}{\chi_{RS} \pi (m+1) \rho_{ref} R_{ref}^k} \right]^{\frac{1}{2+q}} t^{\frac{q+k-2}{2+q}}. \quad (25) \end{aligned}$$

using $R \sim ct$ in the second step. For continuous energy injection into a stellar wind environment ($q = 0$, $k = 2$, $m = 0$), this implies that the ratio between densities at the RS and FS stays constant in time. For a homogeneous circumburst environment ($q = 0$, $k = 0$, $m = 1$), this implies a decreasing density in the RS region 3 relative to FS region 2, with $n'_{RS+}/n'_{FS-} \propto t^{-1}$.

2.4 Typical values for GRB afterglows

We can now plug in some values we expect to be representative of *Swift* afterglows. If the total explosion energy in the blast wave $E_j = 10^{51}$ erg, for a pair of collimated blast waves that start out with collimation angle $\theta_0 = 0.1$ rad., and is injected over the course of $T_{in} = 10^4$ s. at a constant rate ($q = 0$), we have:

$$L = L_0 = E_{iso}/T_{in} = 2E_j/(\theta_0^2 T_{in}) = 2 \cdot 10^{49} \text{ erg s}^{-1}. \quad (26)$$

Here E_{iso} is the isotropic equivalent explosion energy, relevant for radial flow. For a fireball starting at radius $R_0 = 10^{11}$ cm and with $\eta = 300$ (also its peak Lorentz factor), we have a coasting radius $R_L = 3 \cdot 10^{13}$ cm. For these values of η and L the mass loss rate $L_M = 1.18 M_\odot \text{ yr}^{-1}$, with a total mass loss $M = 3.73 \times 10^{-4} M_\odot$ after 10^4 s.

For $q = 0$ and $k = 2$, we obtain¹ $m = 0$, $\chi_{CD} = 1.77$, $\chi_{RS} = 2.51$, $f_{RS+} = 0.379$, $f_{CD} = 0.645$, $g_{RS+} = 1.59$ and $g_{CD} = 1.13$. The fluid profile in the wind case is shown in Fig. 1.

If we take $n_{ref} = 29.9 \text{ cm}^{-3}$ and $R_{ref} = 10^{17}$ cm so that $\rho_{ref} R_{ref}^k = 5 \times 10^{11} \text{ g cm}^{-1}$, which follows for a progenitor stellar wind with velocity 10^3 km s^{-1} and mass loss of $10^{-5} M_\odot \text{ yr}^{-1}$ (Chevalier & Li 2000; Granot & Sari 2002), we then obtain a constant forward shock Lorentz factor $\Gamma = 21.0$ and a RS Lorentz factor $\Gamma_{RS} = 13.3$. In the frame of the inflowing wind (once $R_{RS} > R_L$), we have $\bar{\Gamma}_{RS} = 11.3$, which is indeed relativistic.

For a stellar wind environment the ratio of FS and RS densities determined by eq. 25 is constant and given by $n'_{RS+}/n'_{FS-} = 0.89$.

Using eq. 18 we find that the last of the injected energy at T_{in} is delivered to the blast wave at $T = 3.52 \times 10^6$ s., at which point the outer radius of the explosion is $R = 1.05 \times 10^{17}$ cm. This event is observed (ignoring redshift corrections) at $T_{obs} = T - R_{RS}/c$ (if we take $T_{obs} = 0$ to coincide with the time of the explosion. The expression otherwise merely states that emission departing closer to the observer is seen earlier than simultaneous emission from further distant). It therefore follows that $T_{obs} = T_{in}$ (cf. eq. 17), such that the observed duration of the plateau in *Swift* data can be interpreted directly in terms of duration of energy injection (the argument is analogous to the link between observed variability from internal shocks in the prompt emission and internal engine variability). From this point on the blast wave will evolve into an outflow described by the impulsive energy injection BM solution with energy E_{iso} .

If we take as a measure of the width ΔR of the impulsive energy blast wave the width of a homogeneous shell with density determined by the relativistic shock jump condition at the forward shock and total mass content equal to the total swept-up mass, we obtain $\Delta R = R/[2(3-k)\Gamma^2]$ and $\chi_B = (7-2k)/(3-k)$ for the self-similar position of the back.

If the circumburst medium is homogeneous instead of a free-flowing stellar wind environment, the relative fluid densities of the FS and RS regions are time-dependent. If we use the same explosion energy and injection duration as above but set $n_{ref} = 1 \text{ cm}^{-3}$, typical for values measured assuming a homogeneous interstellar medium (ISM) or stalled wind type environment with $k = 0$, we obtain the following.

The last energy injected at $T_{in} = 10^4$ s. is delivered to the blast wave at $T = 1.07 \times 10^7$ s. At this point the forward shock front is at radius $R = 3.20 \times 10^{17}$ cm. The FS has Lorentz factor $\Gamma = 26.8$, the RS has $\Gamma_{RS} = 16.3$, $\bar{\Gamma}_{RS} = 9.21$. Auxiliary quantities have the values $m = 1$, $\chi_{CD} = 1.81$, $\chi_{RS} = 2.70$, $f_{RS+} = 0.449$, $f_{CD} = 0.709$, $g_{RS+} = 1.48$ and $g_{CD} = 1.10$. At time T , the density ratio between FS and RS is equal to $n'_{RS+}/n'_{FS-} = 0.160$. The ISM fluid profile (at an earlier time than T) is shown in Fig. 2.

¹ In table I of BM76 the corresponding entry for K , setting the square of the FS Lorentz factor, is wrong by a factor $\sqrt{3}$ and should be $K = 1.486$. The same $\sqrt{3}$ term is lacking in their eq. (71), but included in their eqs. (58), (59), (72).

	RS → FS	RS → CD	CD → FS
$k = 2, q = -1/2$	5.05	1.57	3.22
$k = 2, q = 0$	4.05	1.55	2.61
$k = 2, q = 1/2$	3.69	1.54	2.39
$k = 0, q = -1/2$	2.38	1.29	1.84
$k = 0, q = 0$	2.11	1.28	1.65
$k = 0, q = 1/2$	2.01	1.28	1.57

Table 1. Arrival time factors X for arrival at the shock front or CD for sound waves departing from RS or CD. The arrival times themselves are then given by $t_{stop} = X t_{start}$. The factors in the RS → FS column also follow from multiplying the values in the RS → CD and CD → FS columns.

3 TRANSITION AFTER ENERGY INJECTION

After the last energy injected at T_{in} has crossed the reverse shock, the fluid is expected to evolve from the self-similar energy injection profile to the instantaneous energy injection profile at $t \gg T_{in}$. The BM solution is a slow attractor (Gruzinov 2000), which makes it likely that the full transition takes a long time to complete. On the other hand, when we calculate the sound crossing time using the BM solution, the resulting durations are not that long. The co-moving speed of sound is $c_s \equiv 1/\sqrt{3}$ in the relativistic limit, and in the lab frame we have

$$c'_s \approx 1 - \frac{1 - c_s}{1 + c_s} \frac{1}{g(\chi)\Gamma^2} \equiv 1 - \frac{\alpha_s}{g(\chi)\Gamma^2}. \quad (27)$$

Using this value for dr/dt to rewrite dx/dt , we arrive at

$$\frac{dx}{(1 + xQ(x))(2\alpha_s - x)} = (m + 1) \frac{dt}{t}, \quad (28)$$

with $Q(x)$ defined by

$$Q(x) \equiv \frac{(7m + 3k - 4) - (m + 2)x}{(m + 1)(4 - 8x + x^2)}, \quad (29)$$

i.e. the RHS of eq. 12, divided by g . In the impulsive energy case, where $g(\chi) = 1/\chi$, the arrival time t_{stop} at the front ($\chi = 1$), for sound waves departing from χ_{start} at t_{start} , is then given by

$$t_{stop} = \chi_{start}^{\frac{-1}{(1+m)(2\alpha_s-1)}} t_{start}. \quad (30)$$

A sound wave departing from the ‘back’ of the shock χ_B will arrive at $1.35t_{start}$ when $k = 0$, and at $1.55t_{start}$ when $k = 2$. The analytical expression in the energy injection case is less clean, but some results are shown in table 1 for sound waves departing from the RS at $x \equiv 4$ and the CD at $x \equiv 2$. Note also that in the above, the limit $\alpha_s \downarrow 0$ corresponds to replacing c_s by the speed of light, yielding $t_{stop} = \chi_{start}^{\frac{1}{(m+1)}} t_{start}$, for both impulsive and sustained energy injection profiles. This is the absolute minimum amount of time that the front of the shock will remain unaffected by changing conditions at the back. The other limit $\alpha_s \uparrow 1$ corresponds to advective motion away from the shock front(s).

Once the cessation of energy injection has been communicated to the front of the shock, it is expected that the further evolution of the blast wave will start to resemble the impulsive energy injection scenario. The most important characteristics of the blast wave are its Lorentz factor and radius (also in terms of its observational signature, since a

homogeneous shell approximation yields the correct temporal behavior and a flux level that differs from a more detailed approach by a constant factor). When all energy is injected, the shock Lorentz factor will eventually evolve according to (BM76):

$$\Gamma^2 = \frac{(17 - 4k)E_{iso}}{8\pi\rho_{ref}c^{5-k}R_{ref}^k} t^{k-3}, \quad (31)$$

which should be compared to eq. 16. The ratio between the two Lorentz factors, Γ_{FS} from eq. 16 and Γ_I from eq. 31, at time $t = XT_{last}$ (obtaining T_{last} using eq. 18 and X from table 1), is found to be

$$\frac{\Gamma_{FS}^2}{\Gamma_I^2} = \frac{(m + 1)(q + 1)X^{q+1}}{(17 - 4k)f_{RS+}}, \quad (32)$$

which is independent of injection duration, explosion energy and circumburst structure. For $k = 2, q = 0$, we find $\Gamma_{FS}^2/\Gamma_I^2 \approx 1.2$ and for $k = 0, q = 0$ we find $\Gamma_{FS}^2/\Gamma_I^2 \approx 0.55$. It follows that at the time the sound wave reaches the front, the Lorentz factors for the two asymptotic regimes are already comparable. Based on that, no sudden jump or drop in fluid Lorentz factor is expected as the blast wave transits from one regime to the other.

3.1 Dynamical scale invariance

Blast waves with prolonged energy injection exhibit the exact same scale invariance between explosion energies and between circumburst densities as impulsive energy injection blast waves (Van Eerten, van der Horst & MacFadyen 2012; Van Eerten & MacFadyen 2012). The dynamics of the system are fully determined by the parameters $E_{iso} \equiv L_0 T_{in}^{q+1}/(q + 1)$, η , q , k , $A \equiv \rho_{ref} r_{ref}^k$ (unrelated to A from eq. 20), the coordinates r , t , θ and the constant c . The hydrodynamics equations can therefore be written in terms of the variables

$$\left(\frac{E_{iso} t^2}{A r^{5-k}} \right), \quad \left(\frac{r}{ct} \right), \quad \theta, \quad (33)$$

that are scale-invariant under the transformations

$$\begin{aligned} \tilde{E}_{iso} &= \kappa E_{iso}, \\ \tilde{A} &= \lambda A, \\ \tilde{r} &= (\kappa/\lambda)^{1/(3-k)} r, \\ \tilde{t} &= (\kappa/\lambda)^{1/(3-k)} t, \\ \tilde{T}_{in} &= (\kappa/\lambda)^{1/(3-k)} T_{in}, \\ \tilde{L}_0 &= \kappa^{(2-k-q)/(3-k)} \lambda^{(1+q)/(3-k)} L_0. \end{aligned} \quad (34)$$

At early and late times both the flow becomes radial and the variable (r/ct) reduces to 1 and 0 respectively, so that self-similar solutions of a single variable emerge. The scale invariance, however, applies throughout the entire evolution of the blast wave. The resulting scaling for any given fluid quantity depends on its dimensionality, e.g. for the Lorentz factor we have $\tilde{\gamma}(\tilde{r}, \tilde{t}) = \gamma(r, t)$, whereas for the pressure we have $\tilde{p}(\tilde{r}, \tilde{t})/[\tilde{A}\tilde{r}^{-k}c^2] = p/[Ar^{-k}c^2] \rightarrow \tilde{p}(\tilde{r}, \tilde{t}) = \kappa^{-k}\lambda^{k+1}p(r, t)$.

The only addition relative to the impulsive injection scale-invariance from Van Eerten, van der Horst & MacFadyen (2012) is the inclusion of T_{in} , and it should be kept in mind that E_{iso} and T_{in} are not independent parameters. Other than that, the

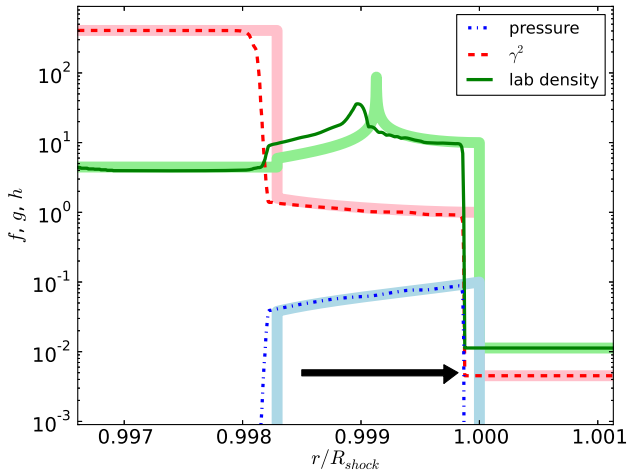


Figure 3. Stellar wind profile for sustained injection scenario ($T_{in} = \infty$), at the time the last energy would have been delivered if T_{in} had been 10^4 s. The direction of the blast wave is to the right. pressure profile p , Lorentz factor-squared γ^2 and lab frame density have been scaled to 10^{-1} , 1, 10 at the FS, respectively. The radius had been scaled to the analytically expected FS radius. Thick light colored lines indicate the analytical solution.

approach from Van Eerten, van der Horst & MacFadyen (2012), where a set of simulations in two dimensions provides the scale-invariant baselines for various jet opening angles θ_0 that are then used for direct comparison to observational afterglow data, can also be applied for energy injection. The extra dimension in parameter space then needs to be accounted for by performing baseline simulations with a fixed E_{iso} but different T_{in} values or, equivalently, a fixed energy injection duration and different luminosities L_0 .

The fact that the scale-invariance for impulsive and prolonged energy injection is identical implies that the full blast wave evolution following T_{last} remains scale-invariant and no additional scaling laws are required to cover the transition to times $t \gg T_{last}$, when the energy injection can be considered as having been instantaneous. In section 4 below I demonstrate that this scale invariance also applies to the synchrotron spectrum directly.

The mass loss rate L_M is linked to the luminosity L via $L_M = L/\eta$, so if the energy flux is scaled, the mass inflow scales accordingly. Different baryon loading gives rise to different dynamics for the free-flowing wind and different density in the reverse shock region.

3.2 Transition Simulations in one dimension

Using the numerical approach described in appendix B, a number of relativistic hydrodynamics (RHD) simulations have been run in one dimension of energy injection into either a wind-shaped or homogeneous environment. In order to test the analytical predictions from the preceding section, four scenario's were explored, corresponding to different combinations of $k = 0, 2$ and $T_{in} = 10^4$ s., ∞ .

In Figs. 3 and 4 fluid profiles have been plotted for the case of sustained energy injection at time $t = T_{last}$ for $k = 0$ and $k = 2$. The radial shifts between the simulation and an-

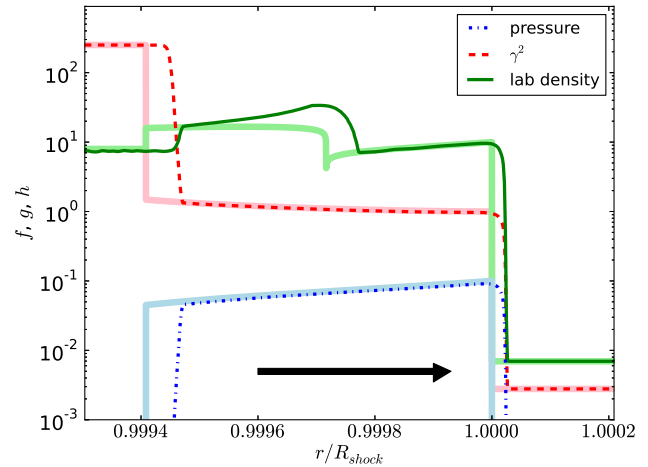


Figure 4. Same as Fig. 3, now for an ISM environment.

alytical fluid profiles that are clearly visible on the plots, are on the order of 10^{-2} percent of the FS radius, and translate to a few percent in terms of the total width of the RS-FS system. Velocity and pressure are reproduced excellently for both wind and ISM scenario's. In the wind case, the infinite spike in mass (where the hot fluid assumption breaks down as well, see section 2.3) can not be reproduced numerically by definition. The reverse shock position is well captured by the analytical solution (accounting for the overall shift). The mass in the RS region (and not in the spike) exceeds the analytical value between 10 - 15 percent. The difference between densities for the simulation with 21 levels of refinement shown on the plot and one with 20 levels is far smaller, so this deviation is likely genuine for these explosion and medium parameters, although part of the explanation lies in the density change across the shock jump for the RS, which tends to be diffused numerically when not manually kept at peak refinement.

In the ISM case, the RS position lies a little ahead of its analytically prediction position (the difference being about twice the overall shift). The RS is captured more sharply, so the jump values for density match better than in the wind case. However, the RS region is smaller while containing the same amount of mass, leading again to higher densities in the simulation profile than analytically predicted. The singularity at the CD is inevitably diffused by the simulation. Nevertheless, both in the wind and ISM case, the profiles demonstrate how the approximate self-similar solution provides a reasonable prediction for the fluid behavior.

In Figs. 5 and 6, we turn to the time-evolution of the blast wave with limited energy injection. The peak pressure is analytically expected at the FS front in both cases, so plotting this quantity provides us with information on the behavior of the shock front. As expected by causality, both plots confirm that the shock front remains unaware of the cessation of energy injection through the RS until after a light crossing time across the RS-FS region. In both cases, the FS does start to deviate from sustained energy injection dynamics slightly before the theoretically predicted times. The discrepancy is most clearly seen in the ISM case, reflecting the fact that the simulation RS-CD-FS profiles are

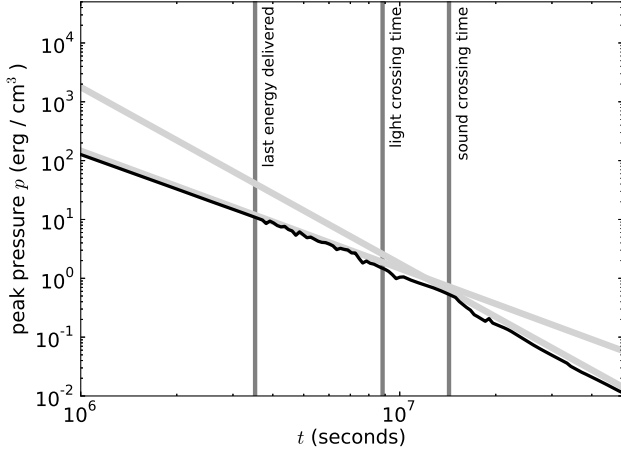


Figure 5. Peak pressure p for a typical blast wave in a stellar wind environment, with limited injection of energy for $T_{in} = 10^4$ s. The peak pressure is analytically expected to occur right behind the FS, and the solid black curve therefore shows the evolution of the FS. The thick grey lines denote the analytical sustained and impulsive energy injection BM solutions. The vertical lines indicate analytically calculated times of potential interest, from left to right: the point where the last energy is delivered across the RS, the point where this event would be communicated to the FS with the speed of light, the point where a sound wave communicating this event reaches the FS.

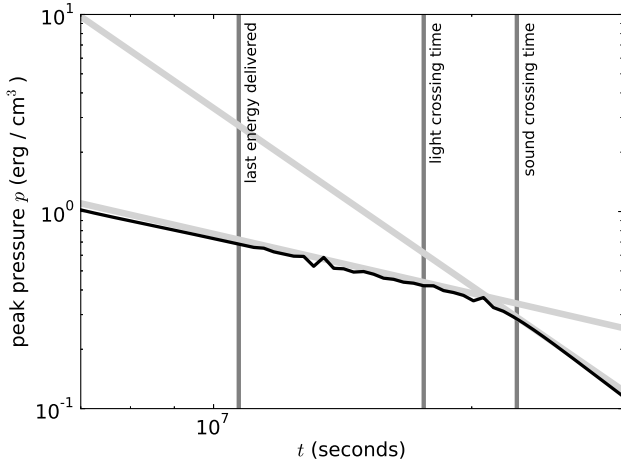


Figure 6. Same as Fig. 5, now for the ISM case.

slightly thinner than analytically predicted, allowing a sound wave to get to the forward shock earlier.

The implications of this for the post-transition fluid profile are shown in Figs. 7 and 8. A small overall shift remains in the ISM case, but no longer in the wind case. The remaining large-scale feature is the FS and the fluid profiles for p , density and γ are all moving to their new asymptotic self-similar values. When looking at the density profile (in green), it can be seen how far this transition is along and the steep drop away from the analytical solution, slightly behind the shock front and seen for both wind and ISM, marks a newly formed CD, separating external fluid shocked since the cessation of energy injection was communicated to the

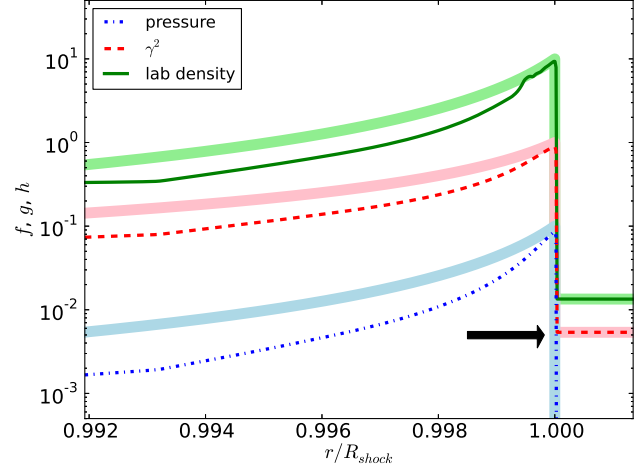


Figure 7. Wind case profile, same as Fig. 3, now for finite energy injection with $T_{in} = 10^4$ s. and taken at the time where a sound wave leaving the reverse shock at the moment of last energy delivery reaches the FS, here 1.43×10^7 s.

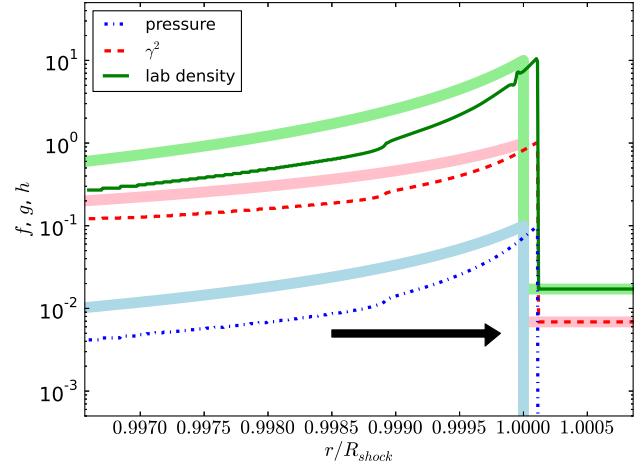


Figure 8. ISM case profile, same as Fig. 4, now for finite energy injection with $T_{in} = 10^4$ s. and taken at the time where a sound wave leaving the reverse shock at the moment of last energy delivery reaches the FS, here 2.26×10^7 s.

front, from previously shocked external medium. Its existence separately confirms that the cessation of energy injection is communicated slightly ahead of the analytically predicted time, given that the snapshot times were chosen to match this predicted time. Across this new CD, pressure and velocity remain continuous, as they should. The ISM case also shows a newly formed RS still within the plot, which runs into the old FS region and communicates backwards the existence of the forward shock (now in a new decelerating phase consistent with impulsive energy injection).

In all, one can estimate the point where the transition is completed fully, to the extent that even the fluid profiles match the impulsive BM solution, as follows. First, take the sound crossing time, then allow for the newly formed CD to advect with the flow until the approximate ‘back’ of the blast wave at χ_B . The latter takes a factor $X = \chi_B^{1/(4-k)}$ to complete (cf. eq. 30). Following constant energy injection

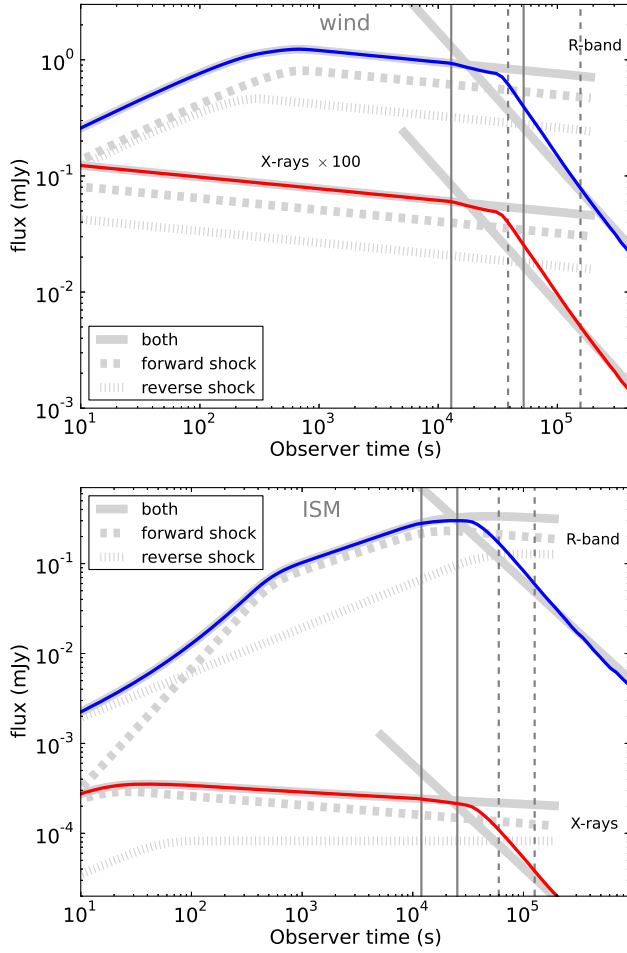


Figure 9. Optical ($\nu = 4.56 \times 10^{14}$ Hz ‘R-band’, upper blue curve) and X-ray ($\nu = 3.63 \times 10^{17}$ Hz, lower red curve) light curves for typical wind (top plot) and ISM (bottom plot) scenario’s. Thick light grey curves plot the analytical solutions for both sustained and impulsive energy injection. Thick dashed light grey curves plot the forward shock region emission only, thick dotted light grey curves the reverse shock region only. From left to right, the grey vertical lines indicate (1) the arrival time of emission from the jet back, sent at the moment when the last injected energy passes through the RS and (2) the arrival time of emission from the jet front, sent at the moment where the last injected energy arrival is communicated to the front via a sound wave. The solid vertical lines are arrival times of emission along the jet axis for these two events, the dashed vertical lines correspond to arrival times of emission from an angle $\theta = 1/\gamma$.

with $q = 0$, this implies that, according to our estimate, the transition is completed at $T_{comp} = 2.11 \times 1.15 T_{last}$ for the ISM case and at $T_{comp} = 4.05 \times 1.22 T_{last}$ for the wind case, where T_{last} the time when the last injected energy crosses the RS, given by eq. 18.

4 LIGHT CURVE PREDICTIONS FOR ENERGY INJECTION FLOWS

In order to link the dynamical energy injection model to GRB afterglow observations, it can be combined with a synchrotron radiation module. In the

afterglow phase, synchrotron emission, by shock-accelerated electrons interacting with local small-scale magnetic fields (presumably also shock-generated), is typically the dominant emission mechanism. In the standard approach (e.g. Meszaros & Rees 1997a; Wijers, Rees & Meszaros 1997; Meszaros, Rees & Wijers 1998; Sari, Piran & Narayan 1998; Wijers & Galama 1999; Rhoads 1999; Granot, Piran & Sari 1999; Gruzinov & Waxman 1999) a fraction $\epsilon_e \sim 0.1$ of the local energy density is assumed to reside in the accelerated electron population, a fraction $\epsilon_B \sim 0.01$ in the magnetic field. A fraction $\xi_N \sim 1$ of the available electrons are assumed accelerated into a power law distribution over energies with slope $-p \sim -2.2$ (see e.g. Curran et al. 2009; Ryan, Van Eerten & MacFadyen 2013, 2014).

In brief, the peak synchrotron flux F_{peak} in the observer frame is proportional to the number of radiating particles and the (comoving) field strength B according to $F_{peak} \propto \Gamma^2 \xi_N n B V$, where the volume of the thin shell $V \propto R^3 / \Gamma^2$. The synchrotron break frequency ν_m in the observer frame is given by $\nu_m \propto \Gamma \gamma_m^2 B$, with $\gamma_m \propto \epsilon_e e / (\xi_N n)$ (the ratio between comoving energy density and number density). In these equations $B^2 \propto \epsilon_B e$. The cooling break frequency in the observer frame $\nu_c \propto \Gamma \gamma_c^2 B$, with $\gamma_c \propto \gamma / (B^2 t)$. Including ν_m and ν_c , but ignoring the synchrotron self-absorption characteristic frequency typically associated with radio emission, the different orderings of observer frequency ν , ν_m and ν_c lead to the observation of different spectral regimes, which in this study are labeled according to:

$$\begin{aligned}
 F_D &\equiv F_{peak}(\nu/\nu_m)^{1/3} & : & \quad \nu < \nu_m < \nu_c, \\
 F_E &\equiv F_{peak}(\nu/\nu_c)^{1/3} & : & \quad \nu < \nu_c < \nu_m, \\
 F_F &\equiv F_{peak}(\nu/\nu_c)^{-1/2} & : & \quad \nu_c < \nu < \nu_m, \\
 F_G &\equiv F_{peak}(\nu/\nu_m)^{(1-p)/2} & : & \quad \nu_m < \nu < \nu_c, \\
 F_H &\equiv F_{peak}(\nu_c/\nu_m)^{(1-p)/2}(\nu/\nu_c)^{-p/2} & : & \quad \nu_m, \nu_c < \nu.
 \end{aligned}$$

This follows the same naming conventions as Granot & Sari (2002); Van Eerten & Wijers (2009).

Both the self-similar solutions and the simulations are used as input for the linear radiative transfer approach to synchrotron emission described in Van Eerten & Wijers (2009); Van Eerten et al. (2010); Van Eerten, Zhang & MacFadyen (2010). In Van Eerten, Zhang & MacFadyen (2010) the exact equations of the implementation used in this paper can be found, and the approach to electron cooling from that paper is applied as well, where we treat the fluid as a single steady-state plasma with a global cooling time (subtleties regarding electron cooling are discussed in Van Eerten 2013 and section 5.1 of this paper).

The dependencies of the flux equations on the model parameters can be calculated analytically for each spectral regime and are tabulated in tables 2 and 3. In these tables, fluxes, frequencies and times are all expressed in the observer frame. In order to translate the observer time t_{obs} , the energy injection duration $T_{in,\oplus}$ and the peak flux to the burster frame where redshift $z = 0$, they need to be divided by $(1+z)$. Frequencies need to be multiplied by $(1+z)$. Note that in Van Eerten & MacFadyen (2012), times and frequencies are expressed in the burster frame in order to

F or ν	scalings	κ (energy)	λ (density)
$F_{peak,I}$	$\frac{(1+z)^{\frac{k-8}{2(k-4)}}}{d_L^2} \xi_N \epsilon_B^{\frac{1}{2}} \left(n_{ref} R_{ref}^k \right)^{\frac{-2}{k-4}} E_{iso}^{\frac{-8+3k}{2(k-4)}} t_{obs}^{\frac{k}{2(k-4)}}$	$\kappa^{\frac{3(k-2)}{2(k-3)}}$	$\lambda^{\frac{-3}{2(k-3)}}$
$\nu_{m,I}$	$(1+z)^{\frac{1}{2}} \xi_N^{-2} \epsilon_e^2 \epsilon_B^{\frac{1}{2}} E_{iso}^{\frac{1}{2}} t_{obs}^{-\frac{3}{2}}$	$\kappa^{\frac{k}{2(k-3)}}$	$\lambda^{\frac{-3}{2(k-3)}}$
$\nu_{c,I}$	$(1+z)^{\frac{4+k}{2(k-4)}} \epsilon_B^{-\frac{3}{2}} \left(n_{ref} R_{ref}^k \right)^{\frac{4}{k-4}} E_{iso}^{\frac{4-3k}{2(k-4)}} t_{obs}^{\frac{4-3k}{2(k-4)}}$	$\kappa^{\frac{4-3k}{2(k-3)}}$	$\lambda^{\frac{5}{2(k-3)}}$
$F_{peak,FS}$	$\frac{(1+z)^{\frac{k-8}{2(k-4)}}}{d_L^2} \xi_N \epsilon_B^{\frac{1}{2}} \left(n_{ref} R_{ref}^k \right)^{\frac{-2}{k-4}} \left(E_{iso} T_{in,\oplus}^{-(1+q)} \right)^{\frac{-(8-3k)}{2(k-4)}} t_{obs}^{\frac{4k-8-8q+3kq}{2(k-4)}}$	same as I	same as I
$\nu_{m,FS}$	$(1+z)^{\frac{1}{2}} \xi_N^{-2} \epsilon_e^2 \epsilon_B^{\frac{1}{2}} \left(E_{iso} T_{in,\oplus}^{-(1+q)} \right)^{\frac{1}{2}} t_{obs}^{\frac{q-2}{2}}$	same as I	same as I
$\nu_{c,FS}$	$(1+z)^{\frac{k+4}{2(k-4)}} \epsilon_B^{-\frac{3}{2}} \left(n_{ref} R_{ref}^k \right)^{\frac{4}{k-4}} \left(E_{iso} T_{in,\oplus}^{-(1+q)} \right)^{\frac{4-3k}{2(k-4)}} t_{obs}^{\frac{-(2+q)(3k-4)}{2(k-4)}}$	same as I	same as I
$F_{peak,RS}$	$\frac{(1+z)^{\frac{3k-14}{2(k-4)}}}{d_L^2} \eta^{-1} \xi_N \epsilon_B^{\frac{1}{2}} \left(n_{ref} R_{ref}^k \right)^{\frac{-1}{k-4}} \left(E_{iso} T_{in,\oplus}^{-(1+q)} \right)^{\frac{3k-10}{2(k-4)}} t_{obs}^{\frac{2k-4-10q+3kq}{2(k-4)}}$	same as I	same as I
$\nu_{m,RS}$	$(1+z)^{\frac{8-3k}{2(k-4)}} \eta^2 \xi_N^{-2} \epsilon_e^2 \epsilon_B^{\frac{1}{2}} \left(n_{ref} R_{ref}^k \right)^{\frac{-2}{k-4}} \left(E_{iso} T_{in,\oplus}^{-(1+q)} \right)^{\frac{k}{2(k-4)}} t_{obs}^{\frac{k(q+2)}{2(k-4)}}$	same as I	same as I
$\nu_{c,RS}$	same as FS	same as FS, I	same as FS, I

Table 2. Flux scalings for the characteristic quantities of the synchrotron spectrum. κ and λ are defined as in Van Eerten, van der Horst & MacFadyen (2012); Van Eerten & MacFadyen (2012).

simplify the equations; the equations here are directly applicable to observations.

Not included in the tables 2 and 3 are the numerical prefactors that fix the absolute flux levels. These have been deferred to appendix C and can be included if one wishes to directly compare model predictions to data.

The dynamical scale invariance in the blast wave dynamics discussed in section 3.1 carries over to light curves, albeit differently for each spectral regime (Van Eerten & MacFadyen 2012). As emphasized in table 2, the energy and density scalings for the impulsive energy injection stage (drawn from Van Eerten & MacFadyen 2013), remain unchanged when considering sustained energy injection instead. A simulation-based evolution curve for any given characteristic quantity, say ν_m , can be scaled to different energies and densities even when it includes a transition from energy injection to impulsive injection: plateau and transition just scale along.

4.1 Application to typical afterglow parameters

The plots of Fig. 9 show optical and X-ray light curves for the typical values of the model parameters discussed in section 2.4. In addition I have taken a redshift $z = 2.23$ (the average *Swift* sample redshift in 2009, see Evans 2009) and

luminosity distance $d_L = 5.6 \times 10^{28}$ cm, but took the value 10^4 for T_{in} s. as referring to the burster frame duration, such that $T_{in}(1+z) = 3.23 \times 10^4$ s. The plots show light curves generated both directly from the analytical solutions for the dynamics and from the numerical simulations that cover the transition stage. For the early emission from the simulations, from before they numerically established the expected self-similar injection profile, analytical fluid profiles were used.

The light curves of Fig. 9 demonstrate a few key points:

(i) **The reverse shock contribution can be significant or dominant.** In our ‘typical’ scenario’s we have assumed the same magnetization for both regions. Even so, the RS flux dominates the FS flux in the optical for 10^2 s in the ISM case, and both flux levels are comparable in the wind case. The magnetization of the FS region is a result from magnetic field generation at the shock front, and to a (presumably) lesser extent, compression of the ambient magnetic field. The original ejecta (i.e. the RS region) can be magnetized to a far higher degree (see e.g. Zhang & Kobayashi 2005; Giannios, Mimica & Aloy 2008; Mimica, Giannios & Aloy 2009). As a result of this difference in magnetization, emission from the RS region can easily be made to dominate the overall flux output, especially when the FS region magnetization is,

regime	scalings
$F_{D,FS}$	$d_L^{-2}(1+z)^{\frac{k-10}{3(k-4)}} \xi_N^{\frac{5}{3}} \epsilon_e^{-\frac{2}{3}} \epsilon_B^{\frac{1}{3}} (n_{ref} R_{ref}^k)^{\frac{-2}{k-4}} \left(E_{iso} T_{in,\oplus}^{-(q+1)}\right)^{\frac{4k-10}{3(k-4)}} t_{obs}^{\frac{7k+4kq-10q-16}{3(k-4)}} \nu^{\frac{1}{3}}$
$F_{E,FS}$	$d_L^{-2}(1+z)^{\frac{k-14}{3(k-4)}} \xi_N \epsilon_B (n_{ref} R_{ref}^k)^{\frac{-10}{3(k-4)}} \left(E_{iso} T_{in,\oplus}^{-(q+1)}\right)^{\frac{6k-14}{3(k-4)}} t_{obs}^{\frac{9k+6kq-14q-16}{3(k-4)}} \nu^{\frac{1}{3}}$
$F_{F,FS}$	$d_L^{-2}(1+z)^{\frac{3}{4}} \xi_N \epsilon_B^{-\frac{1}{4}} \left(E_{iso} T_{in,\oplus}^{-(q+1)}\right)^{\frac{3}{4}} t_{obs}^{\frac{2+3q}{4}} \nu^{-\frac{1}{2}}$
$F_{G,FS}$	$d_L^{-2}(1+z)^{\frac{k-12-4p+pk}{4(k-4)}} \xi_N^{2-p} \epsilon_e^{p-1} \epsilon_B^{\frac{1+p}{4}} (n_{ref} R_{ref}^k)^{\frac{-2}{k-4}} \left(E_{iso} T_{in,\oplus}^{-(1+q)}\right)^{\frac{5k-12-4p+pk}{4(k-4)}} t_{obs}^{\frac{10k+5kq-12q-24-4pq-2pk+8p+pkq}{4(k-4)}} \nu^{\frac{1-p}{2}}$
$F_{H,FS}$	$d_L^{-2}(1+z)^{\frac{2+p}{4}} \xi_N^{2-p} \epsilon_e^{p-1} \epsilon_B^{\frac{p-2}{4}} \left(E_{iso} T_{in,\oplus}^{-(1+q)}\right)^{\frac{2+p}{4}} t_{obs}^{\frac{4+2q-2p+pq}{4}} \nu^{-\frac{p}{2}}$
$F_{D,RS}$	$d_L^{-2}(1+z)^{\frac{3k-13}{3(k-4)}} \eta^{-\frac{5}{3}} \xi_N^{\frac{5}{3}} \epsilon_e^{-\frac{2}{3}} \epsilon_B^{\frac{1}{3}} (n_{ref} R_{ref}^k)^{\frac{-1}{3(k-4)}} \left(E_{iso} T_{in,\oplus}^{-(1+q)}\right)^{\frac{4k-15}{3(k-4)}} t_{obs}^{\frac{2k+4kq-15q-6}{3(k-4)}} \nu^{\frac{1}{3}}$
$F_{E,RS}$	$d_L^{-2}(1+z)^{\frac{k-11}{3(k-4)}} \eta^{-1} \xi_N \epsilon_B (n_{ref} R_{ref}^k)^{\frac{-7}{3(k-4)}} \left(E_{iso} T_{in,\oplus}^{-(q+1)}\right)^{\frac{-17+6k}{3(k-4)}} t_{obs}^{\frac{-17q+6k-10+6kq}{3(k-4)}} \nu^{\frac{1}{3}}$
$F_{F,RS}$	$d_L^{-2}(1+z)^{\frac{3k-8}{4(k-4)}} \eta^{-1} \xi_N \epsilon_B^{-\frac{1}{4}} (n_{ref} R_{ref}^k)^{\frac{1}{k-4}} \left(E_{iso} T_{in,\oplus}^{-(1+q)}\right)^{\frac{-16+3k}{4(k-4)}} t_{obs}^{\frac{-16q-2k+3kq}{4(k-4)}} \nu^{-\frac{1}{2}}$
$F_{G,RS}$	$d_L^{-2}(1+z)^{\frac{-20+5k+8p-3pk}{4(k-4)}} \eta^{p-2} \xi_N^{2-p} \epsilon_e^{p-1} \epsilon_B^{\frac{1+p}{4}} (n_{ref} R_{ref}^k)^{\frac{-p}{k-4}} \left(E_{iso} T_{in,\oplus}^{-(1+q)}\right)^{\frac{-20+5k+pk}{4(k-4)}} t_{obs}^{\frac{-20q+2k-8+5kq+2kp+pkq}{4(k-4)}} \nu^{\frac{1-p}{2}}$
$F_{H,RS}$	$d_L^{-2}(1+z)^{\frac{-32+10k+8p-3pk}{4(k-4)}} \eta^{p-2} \xi_N^{2-p} \epsilon_e^{p-1} \epsilon_B^{\frac{p-2}{4}} (n_{ref} R_{ref}^k)^{\frac{2-p}{k-4}} \left(E_{iso} T_{in,\oplus}^{-(1+q)}\right)^{\frac{-16+2k+pk}{4(k-4)}} t_{obs}^{\frac{-16q-4k+2kq+2pk+pkq}{4(k-4)}} \nu^{-\frac{p}{2}}$

Table 3. Flux scalings for the fluxes in the various spectral regimes.

in turn, weak (see e.g. Kumar & Barniol Duran 2010; Santana, Barniol Duran & Kumar 2013)

(ii) **When the flux contributions from FS and RS region are comparable, the light curve slope will reflect both contributions.** Examples of this are given by the X-ray and optical emission for the typical ISM case and the early time optical emission for the typical wind case.

(iii) **The transition between regimes in the light curve occurs around when cessation of energy injection is communicated to the shock front.** A number of grey vertical lines in Fig. 9 indicate characteristic times for the typical scenario's. A deviation from the sustained energy injection asymptote is first seen when the last of the energy is delivered across the RS. Due to differences in arrival times between different emission angles, the initial change is small. The transition nears completion when the high angle emission is seen that is emitted at time the sound wave from the RS reaches the FS. Here the upper angle is defined by the width of the beaming cone (i.e. $\theta \sim 1/\gamma$; for narrowly collimated ejecta one should use θ_0 instead). The equations

for the two arrival times using the on-axis emission are:

$$\begin{aligned} t_{0,\oplus} &= (1+z)T_{in}/\chi_{RS}, \\ t_{1,\oplus} &= (1+z)T_{in}X/\chi_{RS}, \end{aligned} \quad (35)$$

where X the corresponding factor from table 1. For emission from the edge of the beaming cone, we have:

$$\begin{aligned} t_{0,\oplus} &= (1+z)T_{in}(2m+3)/\chi_{RS}, \\ t_{1,\oplus} &= (1+z)T_{in}X(2m+3)/\chi_{RS}. \end{aligned} \quad (36)$$

These differences in arrival times between on- and off-axis emission are related to the well-known *curvature* effect, putting a limit on the steepness of light curve decay even if the emission were suddenly switched off at the source (see e.g. Kumar & Panaitescu 2000). Once the highest angle emission from the jet edges has arrived, the subsequent drop in flux can be arbitrarily steep.

(iv) **The optical light curve peak does not necessarily mark the onset of the deceleration stage of massive ejecta.** This point was also raised by Leventis, Wijers & van der Horst (2014). In Fig. 9 this is illustrated by the peak at ~ 500 s, which is due to a spectral transition (the passing of ν_m through the observer band),

regime	p, k	$k = 0, \Delta p$	$k = 2, \Delta p$
$F_{D,FS}$	$\frac{k-2}{k-4}$	0.5	0
$F_{E,FS}$	$\frac{3k-2}{3(k-4)}$	0.167	-0.67
$F_{F,FS}$	$-\frac{1}{4}$	-0.25	-0.25
$F_{G,FS}$	$\frac{5k^4-12+12p-3pk}{4(k-4)}$	$-(0.9 + 0.75\Delta p)^b$	$-(1.4 + 0.75\Delta p)$
$F_{H,FS}$	$\frac{2-3p}{4}$	$-(1.15 + 0.75\Delta p)^b$	$-(1.15 + 0.75\Delta p)^b$
$F_{D,RS}$	$\frac{-2k+9}{3(k-4)}$	-0.75^a	-0.833^a
$F_{E,RS}$	$\frac{7}{3(k-4)}$	-0.583	-1.167
$F_{F,RS}$	$\frac{-5k+16}{4(k-4)}$	-1^b	-0.75^a
$F_{G,RS}$	$\frac{12-3k+p}{4(k-4)}$	-0.75^a	$-(1.3 + 0.25\Delta p)$
$F_{H,RS}$	$\frac{16-6k+p}{4(k-4)}$	-1^b	$-(1.05 + 0.25\Delta p)^b$

Table 4. Relation $F \propto t^{\dots}$ between flux F and time t , at the point where $t = T_{in}$, for the different spectral regimes. In addition to the general case with unspecified p and k , the ISM and wind cases are listed separately. In the last two columns, $\Delta p \equiv p - 22/10$ is used to emphasize the value around $p \approx 2.2$. Superscript a marks those entries consistent with the $F_b - t_b$ correlation for optical emission, superscript b marks those consistent with the X-ray $F_b - t_b$ correlation. For both we assumed the range of p to be 2.07 – 2.51 (Ryan, Van Eerten & MacFadyen 2014).

rather than the onset of deceleration.

In addition to the points made above, the flux equations also demonstrate the following:

(v) **RS emission in a wind environment is usually in the fast cooling regime, RS emission in a homogeneous environment in the slow cooling regime.** For slow cooling $\nu_m < \nu_c$, for fast cooling $\nu_c < \nu_m$. In the typical ISM case, $\nu_{m,RS}$ will remain fixed at 1.2×10^{12} Hz, while $\nu_{c,RS}$ will decrease according to $\nu_{c,RS} \propto t_{obs}^{-1}$ and meet ν_m at 1.3×10^7 s $\gg T_{in}$, passing through 1.5 keV at 43 s and the V band at 2.8×10^4 s. This implies that X-ray afterglow light curves (e.g. from *Swift*'s XRT) will have $\nu > \nu_c, \nu_m$, while optical light curves (e.g. from *Swift*'s UVOT) have $\nu_m < \nu < \nu_c$, consistent with the spectral slopes typically found in both regimes (see e.g. Liang et al. 2008; Racusin et al. 2009; Li et al. 2012). It also implies an observationally motivated upper limit on η , given that $\nu_{m,RS} \propto \eta^2$ will easily lead to $\nu_m > \nu$ in the optical, which seems hard to reconcile with reported spectral slopes. For otherwise standard parameters, this limit lies around $\eta \sim 6 \times 10^3$, although this can be offset by a strong decrease in circumburst density or magnetic field strength, according to $\nu_{m,RS} \propto \epsilon_B^{1/2} n_{ref}^{1/2}$, both parameters that are poorly constrained by observations.

In a wind environment, the situation is different. Now, with $q = 0$, it is $\nu_{m,RS}$ that decays according $\nu_{m,RS} \propto t_{obs}^{-1}$, while $\nu_{c,RS} \propto t_{obs}^1$. Typically, $\nu_{m,RS}$ crosses the optical bands around 90 s (which can be mistaken for the onset of deceleration, as mentioned previously). Both frequencies meet at 3×10^3 s, close to the end of the plateau. In this case the strong dependency of $\nu_{m,RS} \propto \eta^2$ means that fast cooling will persist longer, and well past the plateau phase, for larger values of η . If for the X-rays we insist on $\nu > \nu_c, \nu_m$ at least from 10^2 s onward, this implies $\eta < 8 \times 10^3$ for otherwise typical wind parameters.

For $p \sim 2.2$, the shape of the spectrum looks very similar regardless of which critical frequency is highest. Add to this that the RS emission will dissipate post-plateau, leading to

a light curve eventually dictated by an impulsive injection FS, and it follows that conclusions about the nature of the spectrum (i.e. slow vs. fast cooling) at late times can not be automatically extrapolated to early plateau times, such that it becomes hard to dismiss out of hand a fast cooling scenario during the plateau phase.

Finally, combining the observed temporal slopes for X-rays and optical with the flux equations presented here, one finds that the conclusion remains unaltered that observationally $q < 0$ (like -0.5 for a FS analysis, Zhang et al. 2006). In order for the light curve to decay for a wind scenario in fast-cooling regime $F, q < -0.4$.

(vi) **The observational $F_b - t_b$ correlations points to RS emission being dominant during energy injection.** This issue has been discussed by Leventis, Wijers & van der Horst (2014) for homogeneous environments. From measurements of the optical flux F_b at the observed end time t_b of the plateau phase, a correlation $F_b \propto t_b^{-0.78 \pm 0.08}$, has been found (Panaitelescu & Vestrand 2011; Li et al. 2012). In X-rays, a similar correlation but with different negative index $1.07^{+0.09}_{-0.14}$ has been reported (Dainotti et al. 2010, 2013). As the flux equations of table 3 demonstrate, these kind of correlations naturally emerge in a q -independent fashion when the flux is measured at time $t = t_b \sim T_{in}$. At this point in time, all energy is added to the blast wave and the relevant parameters are no longer L_0, q and T_{in} , but E_{iso} instead. In table 4, the dependencies of flux on time when $t = T_{in}$ are listed for all spectral regimes. For the FS emission, these are identical to the impulsive energy injection flux time dependencies; something which naturally follows from dimensional analysis using E_{iso} and t . For the RS emission, the time dependencies are different due to additional dimensionless factors introduced by the density ratio between FS and RS region (cf. eq. 25).

The correlation emerges even across bursts with otherwise differing values for model parameters (E_{iso}, ϵ_B, n_0 , etc.) because selecting the endpoint of the plateau in a sample of bursts means selecting the same point in the scale-invariant characteristic evolution curves (Van Eerten & MacFadyen 2012) for each burst. Possible cross-correlations among L_0, q and T_{in} become irrelevant at this point, since, as stated above, all energy is added to the blast wave. These will therefore not skew the correlation slope. Uncertainties and the intrinsic range of the remaining model parameters will lead to scatter in the correlation, but not impact its slope.

For X-rays we can combine the observed correlation with the observation by Racusin et al. (2009) that during the plateau phase the spectral slope is broadly clustered around -1 (see the distribution for ‘segment II’ in Fig. 2 of the cited paper). This implies that $F(t \sim T_{in}) \propto t^{-1.07} \nu^{-1}$, most consistent with $\nu > \nu_m, \nu_c$. It should be noted here that the spectral transition across the cooling break is very smooth (Granot & Sari 2002; Van Eerten & Wijers 2009; Uhm & Zhang 2014), so the asymptotic power law limit for the slope might not actually be applicable. Regardless, a spectral slope of -1 seems hard to reconcile with the expected slope ~ -0.5 expected when $\nu < \nu_c$. This points us towards the entries for F_H in table 4, where we see that both FS and RS can account for the observed X-ray correlation, both in the wind and ISM case. Out of the four possibilities, RS shock emission for a blast wave running into a stellar wind

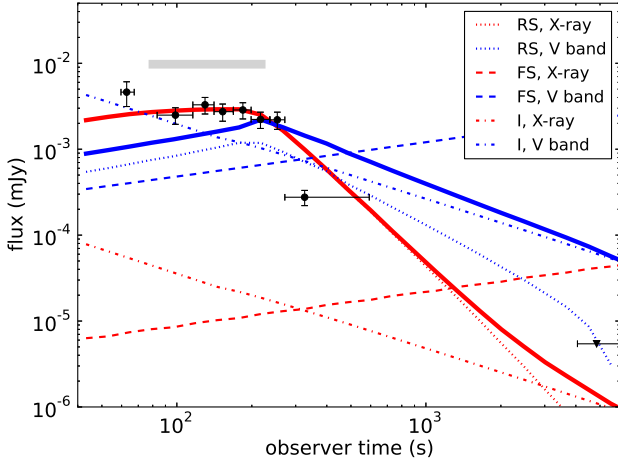


Figure 10. X-ray and R-band light curves for GRB 120521A. The black data points are *Swift* XRT measurements at 1 keV, the horizontal grey bar indicates an optical upper limit. The red curves represent model-based X-rays, the blue curves optical flux. The RS shock contributions are shown by dotted lines, the plateau FS contribution by a dashed lines and the impulsive FS emission by dash-dotted line. The resulting combined fluxes (solid lines) are obtained by adding the RS contribution to the FS contribution, switching between plateau and injected FS when these cross each other. The RS emission is switched off in the lab frame of the explosion once the last injected energy has passed through the RS. The model parameters are $z = 0.4$, $d_L = 6.3 \times 10^{27}$ cm, $E_{iso} = 9 \times 10^{50}$ erg, $T_{in} = 180$ s, $\epsilon_e = 5.6 \times 10^{-2}$, $\epsilon_{B,RS} = 7.9 \times 10^{-3}$, $\epsilon_{B,FS} = 3.2 \times 10^{-6}$, $\xi_N = 1$, $n_{ref} = 2$ cm $^{-3}$, $\eta = 1.1 \times 10^5$, $p = 2.2$, $k = 0$, $q = 0$. The actual redshift for this burst is not known.

environment gives a prediction marginally closer to the observed value than the others. It still depends on p , but this dependency is only weak, $\Delta p/4$, where $\Delta p \equiv p - 2.2$

The optical $F_b - t_b$ correlation is not supported by forward shock emission at all, which presents the strongest argument in favor of emission from the RS region being dominant during the plateau phase. According to table 4, the RS options for the ISM case are $\nu < \nu_m < \nu_c$ (*D*) and $\nu_m < \nu < \nu_c$ (*G*). For the wind case, they are $\nu < \nu_m < \nu_c$ (*D*) and $\nu_c < \nu < \nu_m$ (*F*). The measured spectral slope in the optical is usually negative (see e.g. the collected results in Liang et al. 2008; Li et al. 2012 and references therein; although these values might not fully reflect early plateau time values and evolution of the spectral slope during early times), which, if taken at face value, would rule out *D* and leave us with either the slow cooling (ISM) or fast cooling option (wind). Both would yield a negative spectral slope of 0.5 (assuming $p \sim 2.2$). The reported values from Li et al. (2012) are often consistent with this slope, but also often lie higher, around 0.75. The latter implies either a larger value for p , or that ν approaches the (smooth) spectral break towards spectral regime *H* (i.e. approaches ν_c for ISM or ν_m for wind).

4.2 Application to GRB 090515 and 120521A

In Leventis, Wijers & van der Horst (2014), it is demonstrated how the prolonged energy injection scenario can be

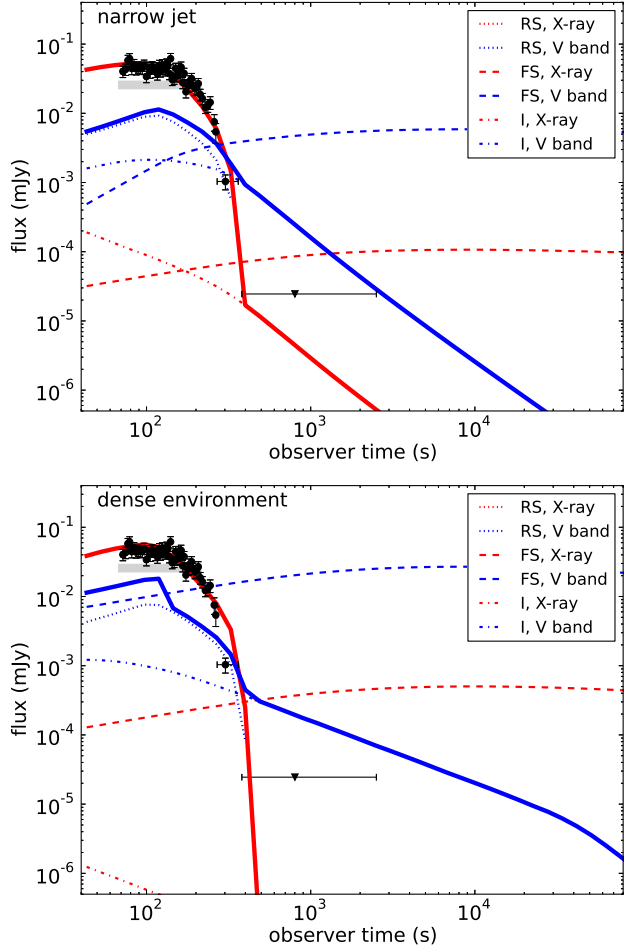


Figure 11. Same as Fig. 10, now for GRB 090515. For the top plot, the model parameters are $z = 0.4$, $d_L = 6.3 \times 10^{27}$ cm, $E_{iso} = 1.2 \times 10^{51}$ erg, $T_{in} = 10^2$ s, $\epsilon_e = 0.5$, $\epsilon_{B,RS} = 3.9 \times 10^{-2}$, $\epsilon_{B,FS} = 10^{-6}$, $\xi_N = 0.79$, $n_{ref} = 0.16$ cm $^{-3}$, $\eta = 2.4 \times 10^4$, $p = 2.2$, $k = 0$, $q = 0$, $\theta_0 = 0.86^\circ$. For the bottom plot, the differing model parameters are $E_{iso} = 2.1 \times 10^{51}$, $T_{in} = 2 \times 10^2$ s., $\epsilon_{B,FS} = 4 \times 10^{-6}$, $\epsilon_{B,RS} = 10^{-9}$, $\xi_N = 1$, $n_{ref} = 9.2 \times 10^4$ cm $^{-3}$, $\eta = 1.2 \times 10^4$, $\theta_0 = 5^\circ$, with n_{ref} dropping to 0.1 cm $^{-3}$ at radii beyond $\sim 6 \times 10^{14}$ cm, associated with the arrival of the last injected energy. These values do *not* represent the best possible fit, but demonstrate a proof of principle. The actual redshift for this burst is not known.

used to explain observations of regular afterglow plateaus, using GRB's 080928 and 090423. To further test the range of the applicability of this type of model we now turn to two more extreme cases, GRB120521A and 090515, characterized by an inferred strong post-plateau decline. A number of recent papers explain short GRB plateaus from a magnetar model (Rowlinson et al. 2010, 2013; Gompertz et al. 2013), and it is instructive to see if these light curves can in principle be accounted for by a RS-FS system, while remaining agnostic about the nature of the power source (it can also be a magnetar-driven FS-RS system, which are argued to have $q = 0$, Dai & Lu 1998; Zhang & Mészáros 2001).

Fig. 10 shows a comparison between BM solution-based light curves and *Swift* XRT data and optical upper limits for GRB 120521A. The synthetic light curves were obtained using the analytical solu-

tion described in section 2 in combination with the synchrotron radiation module from Van Eerten & Wijers (2009); Van Eerten et al. (2010) and the synchrotron prescription from Van Eerten, Zhang & MacFadyen (2010) (as was done at the start of this section). Once the last injected energy passes through the RS, the RS emission is turned off in the lab frame, leading to post-plateau slopes dictated by the curvature effect. In this case I assumed spherical emission, but the flux would be identical for collimated flow unless the jet were very narrow ($\theta_0 < \sim 1^\circ$)

The figure illustrates that it is indeed possible to describe the data using plausible model parameters, if one accepts a low magnetic field for the FS (low being a relative term, these values are fully consistent with e.g. Kumar & Barniol Duran 2010; Santana, Barniol Duran & Kumar 2013). The emission from this burst was argued to require a magnetar origin (as opposed to synchrotron emission from a blast wave) by Rowlinson et al. (2013) based on their inferred steep post-plateau slope and assumed difficulty to account for the optical upper limit from a synchrotron spectrum. Because the inferred steep plateau for this burst is based mainly on a single data point with large error in time, results consistent with the data can also be achieved without equally steep slope. The optical upper limit was considered inconsistent with a synchrotron model based on assuming at most the presence of the cooling break ν_c between optical and X-rays. In our case the issue is avoided by high values for ν_m . As discussed previously, this is naturally expected when RS emission dominates in the plateau phase. For a smooth spectral break, it is not even necessary that $\nu_m > \nu$ in the optical.

The case of GRB 090515, shown in Fig. 11, is more challenging, even though the inferred post-plateau slope is far less extreme than that of GRB 120521A. But here the post-plateau slope is not set by a single data point (although it requires a re-binning of the automatically generated light curve presented on the XRT website to bring this aspect to the surface; for 120521A, the photon arrival times are spread out to much for rebinning to make a difference). The figure presents two alternatives for qualitatively reproducing the features of this burst. In both cases it is necessary to circumvent the limitation on the maximum steepness of the post-plateau slope imposed by the curvature effect (i.e. the spread in arrival times of emission from different angles, even when RS emission ceases at a single lab frame time). Since the curvature effect only applies as long as the jet nature of the outflow is not apparent to the observer, it is necessary that the burst is observed at a time when the blast wave has decelerated at least beyond the point where $\gamma \sim 1/\theta_0$ (see section 5.2 below and e.g. Granot 2007; Van Eerten 2013 for extensive discussions of the nature of jet breaks). In other words, either γ or θ_0 has to be such that this is the case already around 10^2 s.

The top plot of fig. 10 uses a very narrow jet with $\theta_0 = 0.9^\circ$. On the one hand, narrow jets of a few degrees (e.g. five degrees or lower) have actually been inferred for multiple short GRBs (Stratta et al. 2007; Nicuesa Guelbenzu et al. 2012; Fong et al. 2012; Berger 2013). On the other hand, it is not easy to come up with a plausible mechanism to create a narrow jet from a neutron star merger, the preferred scenario for short GRBs.

Short GRBs are often found at an offset from their

host galaxies (see e.g. Fong, Berger & Fox 2010), providing a natural explanation for the low circumburst densities that are often inferred from afterglow modelling (e.g. Belczynski et al. 2006; Berger 2013). It should however be kept in mind that, on the whole, short GRB circumburst densities are poorly constrained due to lack of full broadband coverage (that would need to cover all spectral regimes in order to fully constrain the model). Also, the distance $\sim 10^{13-14}$ cm, covered by the blast wave during the short GRB plateau phase is still very close to the progenitor system and therefore sensitive to its history. When probed at later times and further distant from the source (e.g. $\sim 10^{15}$ cm for GRB 050724, Berger et al. 2005), the local density will more likely resemble the environment density more closely and the effect of density perturbations closer to the source will be negligible compared to the total integrated density that shapes the blast wave evolution. In the bottom plot of fig. 10, I fixed the opening angle of the jet to 5° . The early jet break is now achieved with a circumburst density out to cT_{last} of $n_{ref} = 10^5 \text{ cm}^{-3}$. Integrated over radius, this is about $10^{-5} M_\odot$. Since the Lorentz factor of the outflow is determined by the total amount of swept-up mass, the same effect can be reached by having more circumburst mass within a smaller radius. The total amount of mass remains tiny compared to the $\sim 0.1 M_\odot$ expected to be ejected closely before the merger occurs (see e.g. Rosswog, Piran & Nakar 2013). Once the blast wave pierces the massive shell and emerges in the dilute environment, the FS is expected to speed up essentially instantaneously to a new Lorentz factor dictated by the ratio between the two densities (Gat, van Eerten & MacFadyen 2013).

5 ADDITIONAL DISCUSSION

5.1 Charged particle acceleration and emission

The detailed physics of charged particle acceleration and magnetic field generation in relativistic blast waves and turbulent flows are an incredibly complicated subject that is still poorly understood, and far beyond the scope of this paper. Instead, I have used the (commonly applied) simplifying parameters ϵ_B , ϵ_e and ξ_N , along with some implicit assumptions about their downstream evolution (see Van Eerten 2013 for details). Furthermore, a global approach was used to obtain a single cooling time for the entire plasma, rather than accounting for changing cooling times for fluid parcels as they advect away from acceleration sites. A more detailed treatment will shift the position of ν_c within the RS and FS spectra (see also Van Eerten, Zhang & MacFadyen 2010). Such a treatment, however, would need to address the question at which place(s) electrons are accelerated into a non-thermal distribution. Maybe the dominant process is Fermi shock acceleration at the FS and RS shock fronts. Local cooling could then, in principle, be calculated within the self-similar BM framework using the advection equation 28 from section 3. However, a (relativistic) FS-CD-RS system can easily be Rayleigh-Taylor unstable at the CD (see e.g. Duffell & MacFadyen 2013 for a recent demonstration). Particle acceleration can then also take place throughout the turbulent region, which will spread out through the RS and FS regions.

5.2 sideways spreading

Once causal contact is established among all angles of the collimated blast wave, deviations from radial flow can be expected. This sideways spreading is partially responsible for what is observed as the ‘jet break’ in the afterglow light curve (the other part being the edges of the outflow becoming visible). The onset of spreading can be calculated as the arrival time of a relativistic sound wave moving from edge to tip along a shock front decelerating according to $\Gamma \propto t^{-m/2}$. For nonzero m , this yields $\theta_0 = 1/[(3-k)\Gamma]$ (Van Eerten 2013; MacFadyen & van Eerten 2014). For our typical ISM scenario with $q = 0$ and opening angle 0.1, this leads to $\Gamma = 10$, which puts the onset of spreading well after $\Gamma = 26.8$, when the last energy has been delivered to the shock front. In the typical wind scenario, $m = 0$, so we can not use Γ as a measure of the amount of time that has passed. In this case, $t = t_0 \exp[4\theta_0\Gamma]$, for a sound wave departing from the edge at t_0 . Since $t_0 \sim R_0/c$, causal contact along the shock front is therefore expected already early on during the injection phase.

However, the above does not imply that energy injection blast waves start to decollimate very quickly in the wind case, nor is actual decollimation expected in ISM cases when $\theta_0^{-1} > 26.8$. The reason for this is that the ongoing injection of energy into the blast wave dictates the evolution of the outflow far more than sideways losses. The energy flux in the lab frame, assuming sideways motion with the relativistic speed of sound ($\beta_\perp \sim 1/(4\Gamma)$ in the lab frame), is given by $F \sim \Gamma^2 pc/(4\Gamma)$. For sideways flux along the sides of a homogeneous cylinder of thickness $\Delta R \sim R/(6\Gamma^2)$, this yields an energy loss of

$$\frac{dE}{dt} \sim \frac{(\rho_{ref} r_{ref}^k) c^{5-k} \theta_0 t^{2-k} \Gamma}{24}. \quad (37)$$

Since this is on the order of $10^{41-42} \text{ erg s}^{-1}$ for typical injection scenario’s, it is completely dwarfed by typical source luminosities on the order of $10^{49} \text{ erg s}^{-1}$. If the blast wave decollimates during energy injection, it will be because injection angle θ_0 evolves over time. Otherwise, except for a minor bow shock, the overwhelming bulk of the material will continue along radial flow lines.

In a practical sense, this implies that the results obtained in this paper, both analytical and numerical, are generally applicable even for blast waves that spread out at a later stage and no two-dimensional energy injection simulations are required. Simulation-based fit codes based on templates for impulsive energy injection blast waves (Van Eerten, van der Horst & MacFadyen 2012; Van Eerten & MacFadyen 2012) can be extended to include an energy injection stage by attaching a series of one-dimensional simulation-based templates for various injection durations. As discussed previously in section 3.1, it is straightforward to extend scale invariance to include this stage.

What this does *not* mean, however, is that no jet break-like effect can be seen in the light curve during energy ejection. For nonzero m , there remains the effect of increasing relativistic beaming cone width even while the outflow remains radial. Given that afterglows are typically observed off-axis (Ryan, Van Eerten & MacFadyen 2013, 2014), it is

even likely that the onset of this type of jet break even occurs during the injection phase of the blast wave.

5.3 Energy injection by massive ejecta

There exists an extensive literature on afterglow emission from massive ejecta (e.g. Sari & Piran 1995; Kobayashi, Piran & Sari 1999; Kobayashi & Sari 2000; Ramirez-Ruiz, Celotti & Rees 2002; Wu et al. 2003; Peng, Königl & Granot 2005; Zou, Wu & Dai 2005; Yi, Wu & Dai 2013; Leventis, Wijers & van der Horst 2014). Prolonged energy injection can be understood as a generalization of massive ejecta. In the latter case, the cold ejecta will stratify into a cold wind-type outflow (see also section 2.1) of width $\Delta R \propto R/\Gamma^2$. As long as the RS has not fully crossed the ejecta, this situation is identical to a constant energy input (in the form of ejecta kinetic energy) with $q = 0$ (and in the ‘thick-shell’ case, where the RS becomes relativistic in the frame of the ejecta before completing its crossing, the self-similar profiles described in this paper will also arise). Therefore, the flux equations derived in this paper will reduce to those presented e.g. by Yi, Wu & Dai (2013) if one takes $q = 0$. For ultrarelativistic ejecta, characteristic moments in the ejecta evolution like the completion of the reverse shock crossing and the deceleration radius are expected to occur at timescale $t \ll T_{in}$. Less relativistic massive ejecta, such as the cocoon surrounding the collapsar jet, will have comparable timescales to T_{in} . In that case the RS is likely to remain non-relativistic, so the full self-similar profile will not emerge. Nevertheless, equating the end-time of the plateau to the deceleration time and measuring the flux at this time will pick out the same point in the characteristic evolution across bursts, in the same way as measuring the flux at T_{in} does.

6 SUMMARY

The self-similar forward-shock-reverse-shock (FS-RS) profile arising from a powerful astrophysical source, with luminosity depending on time according to a power law, is studied in detail. A treatment of the density profile and evolution in the reverse shock region is added to the self-similar solution for the fluid profile from Blandford & McKee (1976). The ratio of downstream densities behind the RS and FS remains fixed for constant energy injection into a wind-type environment, and decreases linearly for constant injection into a homogeneous environment. For typical long GRB afterglow parameters, the FS Lorentz factor will be around 20-30 by the end of the plateau stage around 10^4 s , with the Lorentz factor in the wind case having remained unchanged over time. The self-similar fluid profile obeys the same scale invariances as in the impulsive energy injection case (Van Eerten, van der Horst & MacFadyen 2012; Van Eerten & MacFadyen 2012), although the Lorentz factor η of the inflowing ultra-relativistic wind and the coefficient of the power-law luminosity q increase the dimensionality of the parameter space. On the other hand, while impulsive energy injection blast waves with initial half-opening angle θ_0 will undergo sideways spreading once shock Lorentz

factor $\Gamma = (3 - k)^{-1} \theta_0^{-1}$ (Van Eerten 2013), the flow will remain effectively radial during energy injection because the sideways energy flux remains many orders of magnitude below the incoming energy flux through the RS.

The self-similar profile is confirmed by high-resolution numerical simulations of power law injection onto a computational grid. The simulations also confirm that the transition to an impulsive energy injection profile, following the cessation of energy injection, takes about a sound-crossing time. This crossing time can be calculated exactly from the analytical solution.

When combined with a standard synchrotron approach to radiation from shock-accelerated electrons (e.g. Sari, Piran & Narayan 1998), the resulting model dependencies of the flux equations for all spectral regimes of FS and RS emission, as well as the flux levels, can be calculated. These are provided in tables. The flux equations and an application using ‘typical’ afterglow parameters reveal the following properties of the combined emission from these systems:

- The contribution from the reverse shock region can easily be significant or even dominant, certainly when different magnetizations for both regions are taken into account.
- The observed light curve evolution will show a complex interplay between changing FS and RS contributions
- For limited injection duration, the transition from a light curved shaped by sustained injection to one shaped by impulsive energy injection occurs around the point when the cessation of energy injection is communicated to the shock front, although differences in arrival time of emission from different angles will spread out this feature over time.
- Because the synchrotron break frequency ν_m depends quadratically on η for RS emission, it tends to be shifted to high frequencies and can be seen crossing the optical bands during the plateau phase for certain combinations of model parameters.
- RS emission for a blast wave moving into a wind environment tends to be in the fast cooling regime during the plateau stage, while RS emission in the homogeneous case tends to be in the slow cooling regime. Conclusions about the regime based on post-plateau FS emission can not be extrapolated back into the plateau stage when RS emission is dominant at that time. In addition, for a power law distribution of accelerated particles with slope $-p \sim -2.2$, the spectra for both regimes are close to identical.
- The observational optical and X-ray $F_b - t_b$ correlations between flux at the end of the plateau and the plateau duration follow naturally from RS dominated emission. The wind scenario leads to values marginally closer to the prediction, but the difference is very small. The correlation emerges even across bursts with otherwise differing values for model parameters (E_{iso} , ϵ_B , n_0 , etc.) because selecting the end-point of the plateau in a sample of bursts means selecting the same point in the scale-invariant characteristic evolution curves (Van Eerten & MacFadyen 2012) for each burst. At this point, the flux is no longer a function of L_0 , q and T_{in} (but of E_{iso} instead), and possible cross-correlations among these parameters will not skew the correlation slope. Uncertainties and the intrinsic range of the remaining model parameters will lead to scatter in the correlation, but not impact its slope.

Finally, it is shown that the model of synchrotron emission from a blast wave with sustained energy injection up to $\sim 10^2$ seconds can in principle be used to explain short GRBs 090515 and 120521A, that were previously argued to be inconsistent with a synchrotron model and require radiation directly from a magnetar instead (Rowlinson et al. 2013). In our demonstration, a power law slope $q = 0$ was shown consistent with the data. This is actually consistent with energy injection from a magnetar into a FS-RS system, but the generic power law luminosity assumption allows one to remain agnostic about whether or not 090515 and 120521A were caused by magnetars. The sudden cessation of energy injection required in the FS-RS explanation can be understood from a magnetar source. Or it might result from complex fluid behavior once the power law for the luminosity drops below -1, which becomes asymptotically equivalent to impulsive energy injection. The profile at the back end of the injected material can be steepened by rarefaction waves, depending on the shape of the transition.

ACKNOWLEDGMENTS

I wish to thank Antonia Rowlinson and Patricia Schady for assisting with *Swift* data and Kostadinov Leventis, Alexander van der Horst, Paul Duffell and Andrew MacFadyen for helpful discussion. This research was supported in part through Chandra grant TM3-14005X and by the Alexander von Humboldt foundation.

REFERENCES

- Belczynski K., Perna R., Bulik T., Kalogera V., Ivanova N., Lamb D. Q., 2006, *ApJ*, 648, 1110
 Beloborodov A. M., Uhm Z. L., 2006, *ApJ*, 651, L1
 Berger E., 2013, *ArXiv e-prints*
 Berger E. et al., 2005, *Nature*, 438, 988
 Blandford R. D., McKee C. F., 1976, *Physics of Fluids*, 19, 1130
 Blandford R. D., McKee C. F., 1977, *MNRAS*, 180, 343
 Butler N. R., Kocevski D., 2007, *ApJ*, 668, 400
 Chevalier R. A., Li Z.-Y., 2000, *ApJ*, 536, 195
 Curran P. A., Starling R. L. C., van der Horst A. J., Wijers R. A. M. J., 2009, *MNRAS*, 395, 580
 Dai Z. G., Lu T., 1998, *A&A*, 333, L87
 Dainotti M. G., Petrosian V., Singal J., Ostrowski M., 2013, *ApJ*, 774, 157
 Dainotti M. G., Willingale R., Capozziello S., Fabrizio Cardone V., Ostrowski M., 2010, *ApJ*, 722, L215
 Duffell P. C., MacFadyen A. I., 2013, *ApJ*, 775, 87
 Eichler D., Livio M., Piran T., Schramm D. N., 1989, *Nature*, 340, 126
 Evans P. A. e. a., 2009, *MNRAS*, 397, 1177
 Fong W., Berger E., Fox D. B., 2010, *ApJ*, 708, 9
 Fong W. et al., 2012, *ApJ*, 756, 189
 Fryxell B. et al., 2000, *ApJS*, 131, 273
 Gat I., van Eerten H., MacFadyen A., 2013, *ApJ*, 773, 2
 Gehrels N. et al., 2004, *ApJ*, 611, 1005
 Giannios D., Mimica P., Aloy M. A., 2008, *A&A*, 478, 747
 Gompertz B. P., O’Brien P. T., Wynn G. A., Rowlinson A., 2013, *MNRAS*, 431, 1745

- Goodman J., 1986, *ApJ*, 308, L47
- Granot J., 2007, in *Revista Mexicana de Astronomia y Astrofisica Conference Series*, Vol. 27, *Revista Mexicana de Astronomia y Astrofisica*, vol. 27, pp. 140–165
- Granot J., Piran T., Sari R., 1999, *ApJ*, 513, 679
- Granot J., Sari R., 2002, *ApJ*, 568, 820
- Gruzinov A., 2000, *ArXiv: astro-ph/0012364*
- Gruzinov A., Waxman E., 1999, *ApJ*, 511, 852
- Kobayashi S., Piran T., Sari R., 1999, *ApJ*, 513, 669
- Kobayashi S., Sari R., 2000, *ApJ*, 542, 819
- Kumar P., Barniol Duran R., 2010, *MNRAS*, 409, 226
- Kumar P., Panaitescu A., 2000, *ApJ*, 541, L51
- Leventis K., Wijers R. A. M. J., van der Horst A. J., 2014, *MNRAS*, 437, 2448
- Li L. et al., 2012, *ApJ*, 758, 27
- Liang E.-W., Racusin J. L., Zhang B., Zhang B.-B., Burrows D. N., 2008, *ApJ*, 675, 528
- Lyutikov M., Blandford R., 2003, *ArXiv Astrophysics e-prints: 0312347*
- MacFadyen A. I., van Eerten H. J., 2014, manuscript in preparation
- MacFadyen A. I., Woosley S. E., 1999, *ApJ*, 524, 262
- MacNeice P., Olson K. M., Mobarry C., de Fainchtein R., Packer C., 2000, *Computer Physics Communications*, 126, 330
- Mészáros P., 2006, *Reports on Progress in Physics*, 69, 2259
- Meszáros P., Laguna P., Rees M. J., 1993, *ApJ*, 415, 181
- Meszáros P., Rees M. J., 1997a, *ApJ*, 476, 232
- Meszáros P., Rees M. J., 1997b, *ApJ*, 482, L29
- Meszáros P., Rees M. J., Wijers R. A. M. J., 1998, *ApJ*, 499, 301
- Mimica P., Giannios D., Aloy M. A., 2009, *A&A*, 494, 879
- Nakamura K., Shigeyama T., 2006, *ApJ*, 645, 431
- Nakayama K., Shigeyama T., 2005, *ApJ*, 627, 310
- Nicuesa Guelbenzu A. et al., 2012, *A&A*, 548, A101
- Nousek J. A. et al., 2006, *ApJ*, 642, 389
- Paczynski B., 1986, *ApJ*, 308, L43
- Paczynski B., 1991, *Acta Astron.*, 41, 257
- Paczynski B., 1998, *ApJ*, 494, L45
- Panaitescu A., Meszaros P., Rees M. J., 1998, *ApJ*, 503, 314
- Panaitescu A., Vestrand W. T., 2011, *MNRAS*, 414, 3537
- Peng F., Königl A., Granot J., 2005, *ApJ*, 626, 966
- Piran T., 2004, *Reviews of Modern Physics*, 76, 1143
- Piran T., Shemi A., Narayan R., 1993, *MNRAS*, 263, 861
- Racusin J. L. et al., 2009, *ApJ*, 698, 43
- Ramirez-Ruiz E., Celotti A., Rees M. J., 2002, *MNRAS*, 337, 1349
- Rees M. J., Meszaros P., 1998, *ApJ*, 496, L1
- Rhoads J. E., 1999, *ApJ*, 525, 737
- Rosswog S., Piran T., Nakar E., 2013, *MNRAS*, 430, 2585
- Rowlinson A., O’Brien P. T., Metzger B. D., Tanvir N. R., Levan A. J., 2013, *MNRAS*, 430, 1061
- Rowlinson A. et al., 2010, *MNRAS*, 409, 531
- Ryan G., Van Eerten H., MacFadyen A., 2013, 7th Huntsville Gamma-Ray Burst Symposium, GRB 2013: paper 30 in *eConf Proceedings C1304143*
- Ryan G., Van Eerten H., MacFadyen A., 2014, Manuscript in preparation
- Santana R., Barniol Duran R., Kumar P., 2013, *ArXiv e-prints: 1309.3277*
- Sari R., 1997, *ApJ*, 489, L37
- Sari R., Mészáros P., 2000, *ApJ*, 535, L33
- Sari R., Piran T., 1995, *ApJ*, 455, L143
- Sari R., Piran T., Narayan R., 1998, *ApJ*, 497, L17+
- Shemi A., Piran T., 1990, *ApJ*, 365, L55
- Stratta G. et al., 2007, *A&A*, 474, 827
- Thompson C., 1994, *MNRAS*, 270, 480
- Troja E. et al., 2007, *ApJ*, 665, 599
- Uhm Z. L., 2011, *ApJ*, 733, 86
- Uhm Z. L., Zhang B., 2014, *ApJ*, 780, 82
- Uhm Z. L., Zhang B., Hascœt R., Daigne F., Mochkovitch R., Park I. H., 2012, *ApJ*, 761, 147
- Usov V. V., 1992, *Nature*, 357, 472
- Van Eerten H., 2013, 7th Huntsville Gamma-Ray Burst Symposium, GRB 2013: paper 24 in *eConf Proceedings C1304143*
- Van Eerten H., MacFadyen A., 2013, *ApJ*, 767, 141
- Van Eerten H., van der Horst A., MacFadyen A., 2012, *ApJ*, 749, 44
- Van Eerten H., Zhang W., MacFadyen A., 2010, *ApJ*, 722, 235
- Van Eerten H. J., Leventis K., Meliani Z., Wijers R. A. M. J., Keppens R., 2010, *MNRAS*, 403, 300
- Van Eerten H. J., MacFadyen A. I., 2012, *ApJ*, 747, L30
- Van Eerten H. J., Wijers R. A. M. J., 2009, *MNRAS*, 394, 2164
- Wijers R. A. M. J., Galama T. J., 1999, *ApJ*, 523, 177
- Wijers R. A. M. J., Rees M. J., Meszaros P., 1997, *MNRAS*, 288, L51
- Woosley S. E., 1993, *ApJ*, 405, 273
- Wu X. F., Dai Z. G., Huang Y. F., Lu T., 2003, *MNRAS*, 342, 1131
- Yi S.-X., Wu X.-F., Dai Z.-G., 2013, *ApJ*, 776, 120
- Zhang B., Fan Y. Z., Dyks J., Kobayashi S., Mészáros P., Burrows D. N., Nousek J. A., Gehrels N., 2006, *ApJ*, 642, 354
- Zhang B., Kobayashi S., 2005, *ApJ*, 628, 315
- Zhang B., Mészáros P., 2001, *ApJ*, 552, L35
- Zhang W., MacFadyen A., 2009, *ApJ*, 698, 1261
- Zhang W., MacFadyen A. I., 2006, *ApJS*, 164, 255
- Zou Y. C., Wu X. F., Dai Z. G., 2005, *MNRAS*, 363, 93

APPENDIX A: ADDITIONAL SYMBOLS SELF-SIMILAR SOLUTION

For completeness, I define in this appendix some symbols used in expressing the self-similar solution in section 2.2. Straight out of BM76 we have

$$A \equiv \frac{x^2 + 2\alpha_1 x - 8\beta_1}{1 + 2\alpha_1 - 8\beta_1}, \quad B \equiv \frac{(x + \alpha_1 + \gamma_1)(1 + \alpha_1 - \gamma_1)}{(x + \alpha_1 - \gamma_1)(1 + \alpha_1 + \gamma_1)}. \quad (\text{A1})$$

$$\alpha_1 = \frac{m - 3k + 12}{2}, \quad \beta_1 = \frac{m + 1}{2}, \quad \gamma_1 = \sqrt{\alpha_1^2 + 8\beta_1}, \quad (\text{A2})$$

$$\alpha_2 = \frac{-(m + k - 4)}{2}, \quad \beta_2 = \frac{(m - 3k)(m + k) + 8(3m + 4k - 8)}{4}, \quad \gamma_2 = \frac{-(m^2 + 4mk + 3k^2 - 13m - 19k + 24)}{2(m + 3k - 12)}, \quad (\text{A3})$$

$$\mu_1 = \frac{2(7m^2 + 34mk - 118m + 15k^2 - 82k + 96) + (m - 3k + 12)(m^2 + 4mk + 3k^2 - 13m - 19k + 24)}{4(m + 3k - 12)}, \quad (\text{A4})$$

$$\mu_2 = \frac{m - k}{m + 3k - 12}. \quad (\text{A5})$$

In addition to the analytical solution eq. 20 for the density profile, we have for the pressure profile f and Lorentz factor profile g :

$$f = A(x)^{-\alpha_2} \times B(x)^{\beta_2/\gamma_1}, \quad g = A(x)^{\frac{1}{2} + \beta_1} \times B(x)^{[\alpha_1(\beta_1 - 1/2) + 8\beta_1]/\gamma_1}. \quad (\text{A6})$$

APPENDIX B: DESCRIPTION OF NUMERICAL CODE AND SETTINGS

All simulations were performed using the parallel adaptive-mesh refinement (AMR) relativistic hydrodynamics code RAM (Zhang & MacFadyen 2006, 2009). RAM makes use of the PARAMESH amr tools (MacNeice et al. 2000) from FLASH 2.3 (Fryxell et al. 2000). The code allows for various solvers and coordinate systems. For this study, spherical coordinates are used. The RHD equations are solved using a piecewise linear method (a practical approach in the presence of strong shocks). A relativistic equation of state is used with adiabatic index $\Gamma_{ad} = 4/3$ (all relevant parts of the outflow are ultra-relativistic, the BM solution also makes use of this).

The same grid size is used for each simulation. The lower and upper radial boundaries are at 2.998×10^{13} cm (10^3 ls) and 1.499×10^{18} cm (5×10^7 ls) respectively. This grid is divided into 2 base level blocks of 8 cells each and further dynamically subdivided up to 21 levels of refinement (aside from lower refinement consistency checks), where and when needed. As a result, the effective resolution δcell is 8.934×10^{10} cm (2.980 ls). For comparison, the width ΔR of the shell at $t = T_{last}$ is 1.804×10^{14} cm (6.016×10^3 ls) for the typical $k = 2$ case and 1.887×10^{14} cm (6.300×10^3 ls) for the typical $k = 0$ case. The RS-CD-FS system is therefore well resolved at all relevant times. The refinement level of the RS-CD-FS system is manually kept at peak level, while regions at small radii, compared to either the reverse shock radius or the current radius of the last injected energy, are automatically derefined.

The grid is set up with a cold fluid with the appropriate profile (i.e. $k = 0, 2$) and the energy is injected via a boundary condition on the lower boundary, given by eqs. 7. After a time T_{stop} (corresponding to an energy injection duration T_{in} and accounting for the fact that the last injected energy has to be beyond the inner boundary), the luminosity is decreased exponentially according to $L_{drop} = L(\exp[-(t - T_{stop})/(100 T_{stop})] + 10^{-5})$. The mass inflow L_M is equally decreased, while η is kept fixed. As long as the energy injection is decreased sufficiently fast, the exact post-injection evolution of L , L_M and η will not impact the outcome and the current set-up is chosen for numerical reasons.

APPENDIX C: HEURISTIC FLUX FIT FUNCTIONS

The equations in tables 2 and 3 show how the flux depends on the model parameters, but do not give the absolute flux levels. An approximate heuristic function to the flux levels is provided in table C1, calculated from the asymptotic limits for cases where $\nu_m \ll \nu_c$. The lines in this table specify the coefficients α_i of the function

$$C(p, q, k) \equiv \alpha_0 + \alpha_p p + \alpha_k k + \alpha_q q + \alpha_{kq} kq + \alpha_{kk} k^2 + \alpha_{qq} q^2 + \alpha_{pk} pk + \alpha_{pq} pq + \alpha_{kqk} k^2 q + \alpha_{kqq} kq^2 + \alpha_{pqk} pqk + \alpha_{pkk} pk^2 + \alpha_{pqq} pq^2. \quad (\text{C1})$$

For $F_{peak,FS}$, this yields $C(p, q, k) = 8.080 + 0.338p - 3.798k \dots$, etc.

	$F_{peak,FS}$	$\nu_{m,FS}$	$\nu_{c,FS}$	$F_{peak,RS}$	$\nu_{m,RS}$	$\nu_{c,RS}$
pre-factor		$[(2-p)/(1-p)]^2$			$[(2-p)/(1-p)]^2$	
0	7.968	-4.646	-4.136	3.691	0.538	-1.668
p	0.381	0.063	0.122	0.393	0.110	-0.118
k	-3.484	1.522	5.512	-1.173	-2.057	3.984
q	3.577	2.339	-1.565	6.359	-0.065	-2.387
kq	-1.200	-0.696	1.055	-1.751	-0.525	1.525
k^2	0.126	-0.325	-0.443	-0.006	-0.106	-0.234
q^2	0.135	0.101	0.158	-0.720	0.043	0.348
pk	-0.123	-0.099	-0.185	-0.142	-0.158	0.196
pq	-0.029	-0.085	-0.028	-0.030	-0.089	0.074
k^2q	0.004	-0.010	-0.022	-0.008	-0.007	-0.008
kq^2	-0.133	0.045	-0.003	0.150	-0.010	-0.103
pqk	0.016	0.039	0.108	0.024	0.071	-0.043
pk^2	0.022	0.064	0.044	0.026	0.077	-0.048
pq^2	-0.000	0.023	-0.081	0.006	0.017	-0.009

Table C1. Coefficients to heuristic functions for approximating the flux level. See main appendix text for instructions on usage.

	pre-factor	p	k	k^2	pk	pk^2
$F_{peak,I}$	1	4.340	0.508	-2.443	0.133	-0.149
$\nu_{m,I}$	$[(2-p)/(1-p)]^2$	-7.299	0.456	2.192	-0.173	-0.181
$\nu_{c,I}$	1	-2.659	-0.037	4.829	-0.464	-0.338

Table C2. Same as table C1, now for impulsive injection.

The values of the characteristic quantities are then given by

$$\begin{aligned}
F_{peak,FS} &= \text{pre-factor} \times 10^{C(p,q,k)/(4-k)} \frac{(1+z)^{\frac{k-8}{2(k-4)}}}{d_{L,28}^2} \xi_{N,0} \epsilon_{B,-2}^{\frac{1}{2}} \left(n_{ref,0} R_{ref,17}^k \right)^{\frac{-2}{k-4}} \times \\
&\quad \left(E_{iso,53} T_{in,4}^{-(1+q)} \right)^{\frac{-(8-3k)}{2(k-4)}} t_{obs,0}^{\frac{4k-8-8q+3kq}{2(k-4)}} \text{ mJy}, \\
\nu_{m,FS,15} &= \text{pre-factor} \times 10^{C(p,q,k)/(4-k)} (1+z)^{\frac{1}{2}} \xi_{N,0}^{-2} \epsilon_{e,-1}^2 \epsilon_{B,-2}^{\frac{1}{2}} \left(E_{iso,53} T_{in,4}^{-(1+q)} \right)^{\frac{1}{2}} t_{obs,0}^{\frac{q-2}{2}}, \quad (C2)
\end{aligned}$$

et cetera. Here I use the notation $X_{-2} \equiv X \times 10^{-2}$ etc., in cgs units (except for observer time in days), in order to express the characteristic quantities and table entries relative to a given base level. Using the tabulated values will yield the characteristic frequencies in units of 10^{15} Hz (i.e. ν_{15}) and peak fluxes in mJy. The base level values of the model parameters are $d_L = 10^{28}$ cm, $\eta = 1000$, $\xi = 1$, $\epsilon_e = 10^{-1}$, $\epsilon_B = 10^{-2}$, $n_{ref} = 1 \text{ cm}^{-3}$, $R_{ref} = 10^{17}$ cm, $E_{iso} = 10^{53}$ erg, $T_{in} = 10^4$ s, $t_{obs} = 1$ day, hence the notation $E_{iso,53}$, ξ_0 , etc. in eqs. C2 above. Note that these base line values are not always identical to the *typical* values first used in section 2.4.

The heuristic functions have no physical meaning and are merely the combination of a straightforward polynomial divided by the $(4-k)$ factor common to many other terms in the expressions for the characteristic quantities. Their dependence on p is not strong (and only terms up to first order in p are therefore used). In a homogeneous shell model the dependence on p drops out of the characteristic quantity equations completely (see e.g. Leventis, Wijers & van der Horst 2014). Nor does p occur in the exponents of the model parameter dependencies in the characteristic equations for a non-homogeneous profile (see 2). When not ignored in the pre-factors too (e.g. in Van Eerten & MacFadyen 2012, 2013), the residual p -dependency in the pre-factors is the result of the measured characteristic quantities being the weighed average of their values at all simultaneously observed positions in the fluid, with the weighing function being the p -dependent local synchrotron spectrum.

The heuristic functions have been determined by minimizing their differences to the simulation-derived values at all 27 permutations of $k = (0, 1, 2)$, $q = (-0.5, 0, 1)$ and $p = (2.1, 2.5, 3)$. With the values from table C1, the differences always remain at or below 3%.

For comparison, I also provide in table C2 heuristic functions describing the flux level for impulsive energy injection blast waves. These can be combined with flux equations in the various regimes, constructed from table 2 or taken from Van Eerten & Wijers (2009). Note that in Van Eerten & Wijers (2009), a different approach was taken to the synchrotron function, leading to differences in flux levels between that study and table C2.

This paper has been typeset from a \LaTeX file prepared by the author.